



1 **Modelling stress field conditions of the Colima Volcanic Complex**
2 **(Mexico) integrating FEM simulations and geological data**

3
4 Silvia Massaro^{1,2}, Roberto Sulpizio^{1,2,3}, Gianluca Norini², Gianluca Groppelli², Antonio Costa¹,
5 Lucia Capra⁴, Giacomo Lo Zupone⁵, Michele Porfido⁶, Andrea Gabrieli⁷

- 6
7 ¹Istituto Nazionale di Geofisica e Vulcanologia, Via D. Creti 12, 40128, Bologna, Italy.
8 ²Istituto di Geologia Ambientale e Geoingegneria, Consiglio Nazionale delle Ricerche, Via M. Bianco 9, 20131, Milan,
9 Italy.
10 ³Dipartimento di Scienze della Terra e Geoambientali, Via E. Orabona 4, 70125, Bari, Italy.
11 ⁴Centro de Geociencias, Universidad Nacional Autonoma de Mexico, Queretaro, Mexico.
12 ⁵Institute of New Energy and Low-carbon Technology, Sichuan University, Chengdu, PRC.
13 ⁶Alumni Mathematica, Dipartimento di Matematica, Via E. Orabona 4, 70125, Bari, Italy.
14 ⁷Hawai'i Institute of Geophysics and Planetology, 1680 E-W Road, Honolulu, Hawai'i 96922, USA.

15
16 *corresponding author: Silvia Massaro (silvia.massaro@ingv.it)

17 **Abstract**

18 In the last decades numerical methods have become very popular tools in volcanological studies,
19 since capable of considering many relevant parameters in their calculations, such as the presence of
20 multiple reservoirs, topography, and heterogeneous distribution of the host rock mechanical
21 properties. Although the widespread availability of geodetic data is keep growing, the influence of
22 geological data on the numerical simulations is still poorly considered. In this work a 2D Finite
23 Element Modelling is provided by using the commercial Linear Static Analysis (LISA) software, in
24 order to investigate the stress field conditions occurring around the Colima Volcanic Complex (CVC,
25 Mexico) at increasing the details of geological and geophysical input data. By integrating the
26 published geophysical, volcanological and petrological data, we provide a first-order domain of the
27 CVC feeding system, considering either one or two magma chambers connected to the surface via
28 dykes or isolated (not connected) in the elastic host rocks. We test the methodology by using a
29 gravitational modelling with different geometrical configurations and constraints (i.e. magma
30 chamber dimensions, depth, overpressure). Our results suggest that an appropriate set of geological
31 data is of pivotal importance for improving the mesh generation procedures and the degree of
32 accuracy of numerical outputs, aimed to more reliable physics-based representations of the natural
33 systems.

34



35 **1 Introduction**

36 Large-scale deformation of geological systems, characterized by abrupt spatial variations of material
37 properties, was increasingly investigated in recent years through numerical modelling (Xing et al.,
38 2003; Simms and Garven 2004; Manconi et al., 2007; Long and Grosfils 2009; Currenti et al., 2010;
39 Currenti and Williams et al., 2014; Zehner et al., 2015). A large number of semi-analytical and
40 numerical solutions have been proposed, taking into account the static elastic deformation in a multi-
41 layered half-space (Dieterich and Decker, 1975; Bonafede et al., 2002; Wang et al., 2003;
42 Gudmundsson and Brenner, 2004; Zhao et al., 2004; Pritchard and Simons, 2004; Gottsmann et al.,
43 2006; Geyer and Gottsmann, 2010; Zhong et al., 2019). Following the successful application in
44 mechanical engineering, the use of Finite Element Method (FEM) has been extensively introduced in
45 Earth Sciences in order to investigate the effects of topography, lithologic heterogeneities, tectonic
46 stresses and the gravity field on the Earth's surface deformation (Cailleau et al., 2003; 2005;
47 Buchmann and Conolly 2007; Manconi et al., 2009; Pepe et al., 2010; Masterlak et al., 2012; Fujita et
48 al., 2013), including volcanoes (Fujita et al., 2013; Carcho and Sastre, 2014; Bunney 2014; Ronchin
49 et al., 2015; Hickey et al., 2015; Cabaniss et al., 2019; Rivalta et al., 2019). In FEM-based models,
50 the geometry of the Earth's subsurface is performed either by a boundary representation or by
51 discrete cells (Zehner et al., 2015). Boundary representations describe the spatial extent of a geo-
52 object only by its boundaries (Weiler, 1988; Mallet, 1989; Duvinage et al., 1999; Zehner et al., 2015),
53 completely confined and partitioned by surfaces without holes and overlaps. These surfaces can be
54 described as a triangulated surface or by a function like a spline (Mallet, 2002).

55 The use of FEM in volcanic areas has several examples, which vary from the influence of layered
56 materials on the surface deformation process during volcanic inflation (e.g. Darwin volcano,
57 Galapagos Islands; Manconi et al., 2007) to processes affecting chamber rupture (e.g. Grosfils 2007;
58 Long and Grosfils, 2009). The local stress around a volcanic feeding system strongly depends on the
59 magma chamber geometry and on the mechanical properties of the layered host rock around it (Martì
60 and Geyer, 2009). For instance, limestones, lava flows, welded pyroclastic units and intrusions can be
61 very stiff (high Young's modulus), whereas young and non-welded pyroclastic units may be very soft
62 (low Young's modulus). Consequently, the local stress may change abruptly from one layer to
63 another (Gudmundsson, 2006). Irrespective of the scope of the numerical investigation, the



64 importance of applying accurate rheological constraints to FEM modelling was discussed in many
65 studies (Folch et al., 2000; Newman et al., 2001; Fernandez et al., 2001; Currenti et al., 2010; Geshi
66 et al., 2012; Masterlack et al., 2013). This implies that geology of the volcanic area needs to be
67 considered as more accurate as possible. However, few investigations have been carried out to assess
68 the influence of the amount and quality of geological data into FEM computations. To bridge this gap,
69 in this work we use the Linear Static Analysis (LISA) software (version 8.0; www.lisafea.com) to
70 study the subsurface stress behaviour in an elastic domain at Colima Volcanic Complex (CVC,
71 Mexico) when improving the description of geological constraints. In other words, we propose
72 different results of the FEM model by using the available published data of the inferred CVC feeding
73 system structure, in order to assess how the addition of more detailed geological and volcanological
74 constraints may and at what extent affect the model outputs.

75 The CVC area is a good candidate for testing the response of FEM software to different geological
76 conditions, being constituted by a large volcanic complex (significant topographic load; Lungarini et
77 al., 2005), a well-defined feeding system inferred from geophysical and petrological data (e.g. Spica
78 et al., 2017; Massaro et al. 2018; 2019), and growth within a tectonic graben (bordered by normal
79 faults) infilled by volcanoclastic material (variability of rock mechanical characteristics; Norini et al.,
80 2010, 2019).

81 It is worth noting that the elastic models clearly cannot replicate the full complexity of deformation
82 and stress behaviour in volcanic areas if approximations in FEM modelling will not be tested and
83 understood (Grosfils, 2007). Thus, the presented study proposes a contribution to a more proper use
84 of FEM models for assessing surface deformation and failure location patterns in volcanic areas.
85 Beside and beyond the evaluation of geological details on FEM outputs we also obtained a picture of
86 the large-scale stress distribution in the CVC subsurface.

87 Considering the limitations of the results, it is a matter of fact that in volcanic regions many factors
88 make the rocks deviate from pure elastic behaviour and may strongly affect the estimate of source
89 overpressure (Currenti and Williams, 2014). However, although arguably limited in their ability to
90 simulate the complexity characteristics of volcanic areas, elastic models are nonetheless widely used
91 to describe the response of magma reservoir pressure variations and to calibrate the development of
92 more advanced models that enhance our simulation capacities (Grosfils, 2007; Trasatti et al., 2008).



93 **2 The Colima Volcanic Complex (Mexico)**

94 *2.1 Geological framework*

95 The Pleistocene-Holocene Colima Volcanic Complex (CVC) is one of the most prominent volcanic
96 edifices within the Trans-Mexican Volcanic Belt (TMVB) (Macías et al., 2006; Capra et al., 2016;
97 Norini et al., 2019). In this area, the Rivera microplate and the Cocos plate subduct beneath the North
98 America plate along the Middle American Trench, producing great deformation and fragmentation of
99 the continental plate (Stock and Lee, 1994), and forming a triple junction that delimits the tectonic
100 units known as the Jalisco Block (JB) and the Michoacán Block (MB) (Luhr et al., 1985; Allan,
101 1986; Rosas-Elguera et al., 1996; Rosas-Elguera et al., 1997; Ferrari and Rosas- Elguera, 1999;
102 Rosas-Elguera et al., 2003; Frey et al., 2007). The three rifts of this system are the Tepic-Zacoalco
103 (TZR), the Chapala-Tula (CTR), and the Colima Rift (CR) where the CVC is emplaced (Allan 1986;
104 Escudero and Bandy, 2017). The still active NS trending Colima Rift (CR) was formed during an
105 extensional phase occurred after the Late Cretaceous–Paleogene compressive and transpressive phase
106 (Allan, 1986; Serpa et al., 1992; Bandy et al., 1995; Cortés et al., 2010). The rifting phase deformed
107 Cretaceous marine limestones, Jurassic–Tertiary metamorphosed clastic and volcanoclastic sediments,
108 Cretaceous–Tertiary intrusive rocks and Tertiary-Quaternary volcanic deposits along sub-vertical
109 crustal faults. While opening, CR was gradually filled with Pliocene–Quaternary lacustrine sediments,
110 alluvium and colluvium (e.g. Allan, 1986; Allan et al., 1991; Norini et al., 2010). The geometry,
111 kinematics and dynamics of the CR have been studied on the basis of field, seismic, and geodetic
112 data, mainly collected in its northern and central sectors (Fig. 1).

113 The amount of vertical displacement of the northern and central sectors is estimated to be at least 2.5
114 km by adding the topographic relief of the bounding fault scarps (1.5–1.6 km) to the calculated
115 sediment depth (Allan, 1985; Serpa et al., 1992). Field data and focal mechanism solutions are
116 consistent with a direction of opening of the northern and central sectors oriented from E-W to NW-
117 SE, with a mainly normal and minor right-lateral displacements of the bounding faults (Barrier et al.,
118 1990; Suárez et al., 1994; Rosas-Elguera et al., 1996; Garduño-Monroy et al., 1998; Norini et al.,
119 2010; 2019). In contrast to field and seismic evidence of long-term slightly dextral oblique extension,
120 recent GPS geodetic measurements suggest a possible sinistral oblique extension of the CR (Selvans
121 et al., 2011). In both cases, the stress regime is mainly extensional, with an approximately E-W



122 orientation of the minimum horizontal stress in the basement of the CVC (Barrier et al., 1990; Suárez
123 et al., 1994; Rosas-Elguera et al., 1996; Selvans et al., 2011; Norini et al., 2010, 2019).

124 The CVC stands within the central sector of the CR, on top of the Cretaceous limestones, Late
125 Miocene-Pleistocene volcanic rocks, and Pliocene-Holocene lacustrine sediments, alluvium, and
126 colluvium (Allan, 1985, 1986; Allan et al., 1991; Cortes et al., 2005; Norini et al., 2010). The
127 volcanic complex is affected and displaced by the N-S/NNE-SSW-trending recent-active crustal
128 faults of the CR, controlling the geometry and location of the volcano feeding system. Indeed, the
129 CVC was formed by three andesitic stratovolcanoes aligned parallel to the CR bounding faults: the
130 northern inactive Cantaro volcano (2900 m asl), following by the inactive Nevado de Colima (4255
131 m a.s.l.) and, in the southern part, the youngest and active Volcán de Colima (3763 m a.s.l.) (Norini
132 et al., 2019, and reference therein).

133

134 *2.2 Eruptive activity*

135 The eruptive history of the CVC started in the northeast area with the formation of Cantaro volcano
136 at ca. 1-1.5 Ma. The volcanic activity of the Nevado de Colima started at ca. 0.53 Ma. It is composed
137 of voluminous andesitic lava domes and flows and pyroclastic deposits associated with caldera
138 forming eruptions and numerous partial sector collapses (Robin et al., 1987; Roverato et al., 2011;
139 Roverato and Capra, 2013; Cortès et al., 2019). The youngest Volcán de Colima, now considered one
140 of the most active volcanoes of the world, consists of the Paleofuego edifice that suffered several
141 sector collapses, with the formation of a horseshoe-shaped depression where the new active cone
142 (also known Volcán de Fuego) grew up, through Merapi and Soufrière type dome collapses,
143 extrusion of lava flows, Vulcanian and occasionally sub-Plinian explosive eruptions (Saucedo et al.,
144 2010; Massaro et al., 2018, 2019). The activity of both Nevado and Volcán de Colima volcanoes
145 included several sector collapses, occurred frequently in the Upper Pleistocene and Holocene,
146 repeatedly devastating the floor of the Colima Rift down to the Pacific Ocean (Robin et al., 1987;
147 Luhr and Prestegard, 1988; Stoores and Sheridan, 1992; Komorowski et al., 1997; Capra and
148 Macias, 2002; Cortes et al., 2005, 2019; Roverato et al., 2011).

149



150 *2.3 The CVC plumbing system*

151 Spica et al. (2017) indicate a 15 km-deep low velocity body (LVB) as the CVC deep magma
152 reservoir. Its horizontal extension seems to be delimited by the borders of the CR, suggesting a
153 structural control of the normal fault system on it (Spica et al., 2014). The LVB has an extent of ca.
154 55×30 km in the N-S and E-W directions respectively, showing a mean thickness < 8 km. Escudero
155 and Bandy (2017) obtained a higher resolution tomographic image of the subsurface in the CVC area,
156 showing that the most active magma generation zone is presently under the Fuego de Colima edifice.
157 Here, the ambient seismic noise tomographic study proposed by Spica et al. (2014) confirmed the
158 presence of a shallow magma chamber above ca. 7 km depth, as also demonstrated by petrological
159 studies (Medina-Martinez et al., 1996; Luhr, 2002; Zobin et al., 2002; López-Loera et al., 2011;
160 Reubi et al., 2013; 2019; Macías et al., 2017). Cabrera-Gutiérrez and Espíndola (2010) suggested the
161 shallow active magma storage has a volume of ca. 30 km^3 . The shallow magma chamber is
162 connected to the surface by a dyke/conduit system, whose path is facilitated by the presence of the
163 CR fault zone, which provides a natural pathway for fluids (e.g., Allan, 1986; Norini et al., 2010,
164 2019). The arrangement of dykes and the alignment of volcanic centres of CVC suggest that the
165 dykes swarm draining the magma chambers developed along the NNE-SSW-trending, steep,
166 eastward dipping normal fault exposed on the northern CVC flank (Fig. 1) (Norini et al., 2010, 2019).

167 Taking into account the previous information, Massaro et al. (2018) provided a first-order
168 geometrical reconstruction of the Fuego de Colima feeding system during the 1913 sub-Plinian
169 eruption, by using volcanological data (Saucedo et al., 2010, 2011; Bonasia et al., 2011) as input and
170 constraints for numerical simulations. Results showed good matches for a hybrid configuration of the
171 shallow conduit-feeding system (i.e., dyke developing into a shallower cylindrical conduit). The best-
172 fit dyke has width in the range between 200 and 2000 m and thickness of ca. 40 m, with the
173 cylindrical conduit diameter similar to the dyke thickness. The shallow magma chamber top was set
174 at 6 km of depth, and dyke-cylinder transition at 500 m below the summit, as inferred from
175 geophysical data (Salzer et al., 2014; Aràmbula et al., 2018).

176



177 3 Methods

178 In this study, we used the commercial 8.0 version of LISA software (www.lisafea.com). LISA is a
179 general-purpose Finite Element Analysis (FEA) software developed in the '90s based on the
180 formulations proposed by Rao (1989). Since then, formulations from many other sources have been
181 also integrated (Bathe, 1990; Michaeli, 1991; Schwarz, 1991; Babuska et al., 1995). Despite FEA
182 was originally used for structural analysis (Rao, 1989; 2013), it is also able to successfully predict the
183 stress-strain behaviour of rock masses accounting for elastic models, in particular the deformation
184 and failure mechanisms even in layered rock masses (Gabrieli et al., 2015).

185 Simplifying techniques in structural FEA can give valuable insight into local stresses more rapidly
186 and efficiently than a full 3D model. Here we considered a 2D model throughout a complex structure,
187 in order to investigate the stress behaviour induced in the host rocks in response to the increasing
188 detail of geological data used to constrain the model.

189 3.3 Modelling approach

190 Taking into account the works of Norini et al. (2010, 2019), we simulated the deformation of the
191 CVC plumbing system considering an E-W cross section, which is parallel to the extension
192 associated to the active Colima Rift (Norini et al., 2010), shown in Figure 1a (a-a').

193 Since the extensions of the CVC magma chambers in the NNE-SSW direction are typically much
194 longer than the dimensions of the E-W cross section (Spica et al., 2017), 2D solutions of either
195 numerical or analytical models describing E-W elongated magma chambers in the crust can be
196 legitimately adopted (Jaeger et al., 2007; Costa et al., 2011). A topographic profile and 2D plane
197 along the chosen E-W cross-section of the CVC area was obtained in ESRI ArcGIS from a Digital
198 Elevation Model (DEM; resolution 50 m; INEGI website). This cross section was imported into
199 Autodesk Auto-Cad R13 and approximated to a third-degree spline. Finally, the IGES file was
200 imported into LISA, where the mesh discretization was performed. The domain was discretized by
201 three-noded triangular finite elements (Table 1).

202 The volcanic area domain extends 60 km horizontally and 30 km below the surface set in an x - z
203 Cartesian Coordinate System. Zero normal displacements are assigned at the bottom and the lateral
204 boundaries of the domain, while the upper boundary representing the ground surface is stress free.



205 FEM of geological structures requires accurate discretization of the computational domain such that
206 geological units are represented correctly. Zehner et al. (2015) reported that the unstructured
207 tetrahedral meshes on a complex geological model has to fulfil the following requirements: i)
208 sufficient mesh quality: the tetrahedrons should not be too acute-angled, since numerical instabilities
209 can occur, ii) incorporation of geometry for defining boundary conditions and constraints, iii) local
210 adaption, which is a refinement of the mesh in the vicinity of physical sources in order to avoid
211 numerical errors during the simulation. Considering these requirements, in this work we adopt as the
212 best discretization a mesh with 4660 elements for the E-W cross-section (Table 1). The size of finite
213 elements was refined in the regions with higher gradients, especially near the contours of the
214 magmatic feeding systems.

215 In our simulations, the geometry of the geological units is referred to the model in Norini et al. (2010,
216 2019). Magma chambers and dykes are considered as finite-size bodies in an elastic crustal segment,
217 acting as fluid-filled holes. This approach has been extensively used in several analytical and
218 numerical models that treated magma reservoirs as internally pressurized ellipsoidal cavities within
219 an elastic half space, in order to gain insight into the behaviour of magma plumbing systems (Pinel
220 and Jaupart, 2004; Gudmundsson, 2006; Grosfils, 2007; Andrew and Gudmundsson, 2008;
221 Hautmann et al., 2013; Currenti and Williams, 2014; Zhong et al., 2019).

222 The geometrical configuration set for the CVC feeding system (i.e. the shape and dimensions of the
223 magmatic chambers) derives from literature (Spica et al., 2014, 2017; Alvarez and Yutzis, 2015,
224 Massaro et al., 2018, 2019). The overpressure in magma chambers may be produced by a variety of
225 processes, including fractional crystallization, volatile exsolution and magma recharge, leading to
226 deviatoric stresses in the country rock that may be tens of MPa in magnitude (Jellinek and DePaolo,
227 2003; Karlstrom et al., 2010).

228 Previously published studies indicate that differences between and problems with elastic models
229 derive principally from the key role played by gravity. Gravity plays a first order role on bedrock
230 failure conditions (Gerbault, 2012), on the geometry of magma propagation with respect to an edifice
231 load (Corbi et al., 2015) and on buoyancy contrasts driving magma upward (Lister and Kerr, 1991;
232 Watanabe et al., 2002). However, in a wide variety of simulations of natural phenomena the



233 gravitational effects are often incorporated either incorrectly or incompletely (Grosfils, 2007). Some
234 authors argued on whether it is appropriate or not to account for the gravity body force in numerical
235 models of volcanic inflation (Currenti and Williams, 2014; Grosfils et al., 2015). When the
236 gravitational loading is not included in the model, the volcanic deformation results from a change
237 with respect to a stage previously at equilibrium (Gerbault et al. 2018).

238 In this work, we carried out simulations considering the effect of the gravitational loading. Gravity in
239 the host rock ($z \leq 0$ m) is implemented via body forces and the application of a lithostatic stress.

240

241 **4 Geological data**

242 In this work, we used geological information available in literature as input data, in order to estimate
243 the stress variations around the CVC magmatic plumbing system. Here we briefly describe the main
244 geological features taken into account in LISA simulations.

245 *4.1 Stratigraphy*

246 Five units forming the CVC system were defined from the available geological data (Table 2): i)
247 *Basement (Unit B)*: cretaceous limestones and intrusive rocks forming the bed-rock underlying the
248 CVC; ii) *Graben fill deposits (Unit GF)*: Quaternary alluvial, colluvial, and lacustrine deposits filling
249 the graben; iii) *Fuego de Colima deposits (Unit FC)*: andesitic lavas and pyroclastic deposits forming
250 the Paleofuego-Fuego de Colima edifices; and iv) *Volcaniclastic deposits (Unit VD)*: volcaniclastic
251 deposits covering the southern flank of the CVC (e.g. Cortés et al. 2010; Norini et al., 2010, 2019).
252 Being the area interested by FEM extended down to 30 km, it is evident how *Unit B* is dominant with
253 respect to the others, which occupy only few km in the upper part of the simulated domain. We
254 assumed constant mechanical characteristics within each Unit (Table 2). In particular, *Unit B* was
255 considered mechanically homogeneous with elastic properties of a carbonate, due to the lack more
256 detailed information of deeper lithologies (Norini et al., 2019).

257 Deformation within the brittle upper crust is described by elastic material behaviour. For each Unit
258 we fixed typical rock mass properties, density (ρ), Young's Modulus (E) and Poisson's Ratio (ν)
259 (Table 2). The rock masses are considered dry, in order (eventual) pore pressure to be neglected.



260 Only for *Unit GF* a higher value for the Poisson's Ratio was used close to the surface in order to
261 mimic high water content in the graben sediments. The maximum thickness of the graben fill (about
262 1 km) was assumed from the literature (Allan, 1985; Serpa et al., 1992; Norini et al., 2010, 2019). For
263 Units B and GF rock mass proprieties were derived from Hoek and Brown (1997) and Marinos and
264 Hoek (2000), while for volcanic materials (units *FC* and *VD*; Table 2) were estimated according to
265 the approach proposed by Del Potro and Hürlimann (2008). This information allowed Norini et al.
266 (2019) to derive the equivalent Mohr-Coulomb properties for the stress ranges expected in the
267 different sectors of the CVC.

268

269 *4.2 The geometry of the plumbing system*

270 The geometry of the E-W cross-section of the CVC plumbing system was modelled taking into
271 account the previous subsurface information described in Section 4.1. In our 2D model, we assumed
272 the CVC composed of a two magma chambers connected by dykes and to the surface by a conduit.
273 The shape of the magma chambers and dykes are represented by elliptical cross-sections with the
274 major ($2a$) and minor ($2b$) axes over which magmatic overpressure (ΔP) acts.

275 Generally, the magma chambers have a sill-like shape that is often imaged in seismic studies of
276 volcanoes and rift zones (Macdonald, 1982; Sinton and Detrick, 1992; Mutter et al., 1995; MacLeod
277 and Yaouancq, 2000; Singh et al., 2006; Canales et al., 2009). Most of them are not totally molten
278 but rather a mixture of melt and crystal mush (i.e. Parfitt and Wilson, 2008). Various estimates have
279 been made to infer the actual amount of melt in a magmatic body, showing that it is only ca. 10% of
280 the total chamber volume (Gudmundsson et al., 2012 and reference therein).

281 Spica et al. (2017) described a 15 km-deep low velocity body (LVB) with its top at ca. 15 km of
282 depth and with an estimated volume of ca. 7000 km^3 , representing the deep magmatic reservoir of

283 CVC. Assuming the melt as 10%, the deep magma chamber volume would be ca. 700 km^3 .

284 Simplifying this volume in an elliptical sill-like geometry, the dimensions (i.e. $2a$, $2b$, $2c$ axes) have
285 to be scaled according to those of LVB ($55 \times 30 \times 8 \text{ km}$; Spica et al., 2017). We therefore fixed $2a =$
286 14 km , $2b = 3.6 \text{ km}$, $2c = 26 \text{ km}$ as dimensions of the deep magma chamber, being $2c$ elongated in



287 NW-SE direction.

288 For the shallow part of the feeding system, we have no detailed geophysical constraints. However,
289 Massaro et al. (2019) reproduced through numerical modelling the nonlinear cyclic eruptive activity
290 at Fuego de Colima in the last 20 years, using a shallow magma chamber volume in the range of 20-
291 50 km^3 , also according to the estimation of Cabrera-Gutiérrez and Espindola (2010). Assuming a
292 volume of 30 km^3 , we fixed $2a = 3.5 \text{ km}$, $2b = 2 \text{ km}$, $2c = 8 \text{ km}$ as dimensions of the shallow magma
293 chamber.

294 Numerous theoretical and field studies have established that host rock stresses dictate the magma
295 pathways (e.g. Maccaferri et al., 2011; Gudmundsson 2011). During ascent to the surface, the dykes
296 align themselves with the most energy-efficient orientation, which is roughly perpendicular to the
297 least compressive principal stress axis σ_3 (e.g. Gonnermann and Taisne, 2015; Rivalta et al., 2019).
298 This behaviour, however, can be modulated in the presence of significant variations in fracture
299 toughness of the surrounding rock due to stratification (Maccaferri et al., 2010) or to old and inactive
300 fracture systems (Norini et al., 2019). Although for oblate magma chambers the propagation of dykes
301 is most probable from the tip areas, in our simulations the orientation of dykes is assumed vertical,
302 because of the preferential pathways represented by the CR fault planes (Spica et al., 2017).

303 Although, for decades, magma conduits were modelled as cylinders, because of easiness of their
304 mathematical treatment, geophysical data and field observations highlight the importance of dykes in
305 magma transport and hence the need to adopt more realistic geometries (Costa et al., 2009; Hautmann
306 et al., 2013; Tibaldi, 2015). It is important to stress that although all cavities/inclusions in a medium
307 modify the local stress field and concentrate stresses, the induced perturbation depends mainly on the
308 geometry of the cavity/inclusion (Savin, 1961; Borelli and Sidebottom, 1985; Tan, 1994; Saada,
309 2009). We set the dimensions of feeder dykes in agreement with Massaro et al. (2018): deep dyke $2ad$
310 $= 2 \text{ km}$; shallow dyke $2a$ varies from 1 km at bottom to 500 m in the upper part of the volcano; width
311 of both deep and shallow dyke $2bd = 2b = 100 \text{ m}$.

312 It is worth noting that it is not the aim of this study to provide the conditions for the magma chamber
313 rupture, being LISA accounting only for the elastic regime. For these reasons, the selected magma
314 overpressures (ΔP) have to be less than the tensile strength of the rocks. We therefore fixed ΔP at



315 10 MPa and 20 MPa for the 15 km-deep chamber, and 5 MPa for the 6 km-deep one. For the
316 modelling of the dyke and conduit the magmatic overpressure is fixed at 10 MPa in the deeper dyke
317 and 5 MPa in the shallower dyke, except for the upper 500 m of the shallower dyke where
318 overpressure is set at 0.4 MPa.

319

320

321 **5 Results**

322 The first part of this section is focused on sensitivity analysis of Young modulus variation, aimed to
323 quantify the numerical effects of approximation of this important rock property on FEM outputs.
324 The second part of this section describes the model when adding complexity to the input
325 geological/geophysical data.

326 Considering the E-W cross-section (a-a'; Fig. 1a), we provided six domain configurations with
327 increasing geological complexity: i) “*homogeneous lithology model*” in which the volcanic domain is
328 only composed of andesite rocks; ii) “*not homogeneous lithology model*” where different geological
329 units are considered; iii) “*single magma chamber model*” composed of a not homogeneous lithology
330 and a 15 km-deep magma chamber; iv) “*dual magma chamber model*” composed of a not
331 homogeneous and 6 km- and 15 km-deep magma chambers; v) “*feeding system model*” composed of
332 not homogeneous lithology, 6 km- and 15 km-deep magma chambers connected through a deep-dyke,
333 and a shallow conduit connecting to the surface; vi) “*extensional model*”, in which we added a 5 MPa
334 horizontal extensional stress to configurations ii) – v) (Fig. 1b).

335

336 *5.1 Sensitivity analysis on selected input parameters*

337 In order to quantify the influence of Young Modulus selection on the model outputs, we performed a
338 sensitivity test using the single magma chamber model as reference case. We evaluated the influence
339 of varying the Young Modulus in each geological Units on the principal stresses σ_1 and σ_3 . Taking
340 into account the material properties used in the simulations (Norini et al., 2010, 2019; Table 2) as
341 reference values, we compared the stress state of the computational domain at changing (\pm) Young



342 Modulus by an order of magnitude. This variation has been separately applied to each Unit, in order
343 to assess what is the effect of changing material properties on model outputs. This sensitivity analysis,
344 although incomplete, may lead to raise awareness on the selection of input data when running a FEM.
345 The sensitivity analysis was carried out on a reduced simulation domain, in order to diminish the
346 influence of binding effects that are present along domain borders.

347 We used the Euclidean norm (L2) method for illustrating the results of the sensitivity analysis. The
348 L2 norm applied on a vector space x (having components $i = 1, \dots, n$) is strongly related with the
349 Euclidean distance from its origin, and is equal to:

350

$$351 \quad ||x||_2 = \sqrt{\sum_i^n x_i^2} \quad (1)$$

352

353 In our case, the vector space x is composed of all nodes of the computational domain (Table 1). We
354 defined x_{ref} the vector containing the results for the maximum and minimum principal stress when
355 using the selected values of material properties (Table 1) and $x(-)$, $x(+)$ the vectors at varying the
356 Young Modulus of one order of magnitude in each Unit.

357 We evaluated the global variation of stress in the proposed geometrical configurations of the domain
358 (i.e. not homogeneous lithology, single magma chamber, dual magma chamber, and dual magma
359 chamber with conduits models) calculating the global relative variation in L2 as follow:

360

$$361 \quad L2(-) = \frac{||x_{ref} - x(-)||_2}{||x_{ref}||_2} \quad (2)$$

$$362 \quad L2(+) = \frac{||x_{ref} - x(+)||_2}{||x_{ref}||_2} \quad (3)$$

363

364 In Figure 2 are reported the global relative variations in L2 of the principal maximum stress σ_1 and
365 principal minimum stress σ_3 caused by the variation of Young Modulus in each Unit. All the
366 geometric configurations show variability less than 15%, with few exceptions within *Unit B* that have
367 variability over 30% (Fig. 2; Table 3). It is worth noting that the spatial distribution of the major
368 variations seems to not significantly affect the final stress distributions, because: i) they are located



369 near the mesh borders (Fig. 3a, b); and, ii) when not at the mesh borders, the variations are limited to
370 few % (Fig. 3c, d). It means that changing the Young Modulus of one order of magnitude produces
371 variation in FEM outputs distributed over a large domain and the change affecting the single nodes is
372 limited to few %.

373

374 *5.2 Homogeneous and not homogeneous lithology*

375 We carried out LISA simulations considering the effect of the gravitational loading on the
376 homogeneous and not homogeneous lithology on FEM outputs. In Figure 4 we reported a gravity
377 loading model for E-W cross-section of the CVC system. We first considered the homogeneous rock
378 composition composed by only andesitic lavas (Fig. 4a) and then by carbonates (*Unit B*), alluvial,
379 volcanoclastic and pyroclastic deposits (*Units GF* and *VD*; Fig. 4b). We analysed the principal
380 stresses σ_1 and σ_3 acting on the system, which correspond to the maximum and minimum stress at
381 a point, respectively.

382 Figure 4 shows the patterns of the minimum principal stress σ_3 (panels i-ii) and of the maximum
383 principal stress σ_1 (panels iii-vi), highlighting very slight differences between the homogeneous and
384 not homogeneous lithology cases. It is very important to stress that the x - z zero displacement
385 assigned at the bottom and the lateral boundaries of the domain created substantial artefacts in the
386 results (i.e. curved patterns of stress). The artefacts are also evident when considering σ_3 (panels i-ii)
387 where the boundary effect on x -axis is amplified by the presence of the upper free surface. For this
388 reason, the only area to be considered as unperturbed is the central part of the entire domain, and it
389 extends ca. 30 km horizontally and ca. 15 km vertically (within the blue contour in Fig. 4).

390

391 *5.3 Gravitational modelling using the inferred feeding system geometry*

392 We progressively add the elements of the conduit/feeding system of the CVC to FEM under the
393 effect of the gravitational loading. Three cross-section profiles (Figs. 5, 6) show increasing
394 complexity of the feeding system starting from a single magma chamber, passing to two magma
395 chambers and, finally, adding the conduits.

396 Figure 5a describes the distribution of the minimum principal stress σ_3 (panel i) and the maximum



397 principal stress σ_1 (panel ii) at magma chamber overpressure of 10 MPa, showing how the insertion
398 of the pressurized magma chamber modifies the lithostatic stress. No significant differences in
399 magnitude and pattern of stresses are visible when having a magma chamber overpressure of 20 MPa
400 (Appendix 1a).

401 The addition of the shallow magma chamber significantly changes the values and pattern of both σ_3
402 and σ_1 (Fig. 5b). In particular, σ_3 and σ_1 stresses describe a typical inflation pattern produced by
403 overpressurised magma chamber(s) (Anderson, 1936; Gudmundsson, 2006), producing well-defined
404 stress arches of σ_3 (red dotted lines in Figs. 5bi) and divergent strong gradients of σ_1 , well developed
405 around the larger magma chamber (Fig. 5bii). Stress arch is a common phenomenon occurring in
406 continuous materials as response to applied pressure. It has been proved to have great influences on
407 the self-stabilization of soils or rock masses (Huang and Zhang, 2012), and may influence
408 mechanisms of caldera collapse (Holohan et al., 2015). Very slight differences in magnitude and
409 pattern of stresses appear when using 10 MPa (Fig. 5b) or 20 MPa of deep magma chamber
410 overpressure (Appendix 1b).

411 Figure 6 shows the addition of two conduits connecting the deep and shallow magma chambers. It is
412 evident how the insertion of the conduits in the feeding system of CVC dramatically changes the
413 stress distribution, with disappearance of the stress arch and an almost constant stress in the
414 computational domain except than on the tips of the deep magma chamber.

415

416 *5.4 Addition of an extensional field stress*

417 In order to explore the influence of the extensional field stress on stress patterns caused by the
418 presence of the CR (Fig. 1a), we run simulations applying 5 MPa of extensional stress to the FEM
419 domain, which is a typical value for rift zones (Turcotte and Schubert, 2002; Moek et al., 2009;
420 Maccaferri et al., 2014; Sulpizio and Massaro, 2017). This should reproduce the effect of the CR on
421 the different feeding system configurations (Fig. 7).

422 In the case of a single magma chamber (with 10 MPa overpressure), the addition of extensional far
423 field stress reduces the confinement effect due to the no displacement condition imposed along the x-



424 z directions. The effect of the extensional field stress on double magma chamber configuration (with
425 10 MPa overpressure in the deep chamber and 5 MPa in the shallower one) produces slight changes
426 in stress magnitude and pattern for both σ_3 and σ_1 (Fig. 7). The same applies also for the complete
427 feeding system configuration, in which the attrition of the far field stress changes slightly the
428 intensity of the stresses and patterns. Using 20 MPa overpressure in the deep magma chamber does
429 not significantly affect the model outputs (Appendix 2).

430

431 **6 Discussions**

432

433 *6.1 FEM analysis at increasing geological details*

434 The presented FEM model of the CVC highlighted some important characteristics of crustal stress
435 distribution at changing geological constraints used as input conditions (Spica et al. 2014; 2017;
436 Massaro et al., 2018). Although the results have to be considered as a first order approximation, the
437 changes in stress distribution are evident and useful for the understanding of limitations and
438 advantages of finite element modelling.

439 We used the conditions of gravitational loading, the zero-displacement along x - z directions and
440 overpressured magma chambers and dykes in order to simulate the fluid state conditions. Under these
441 assumptions, the use of homogeneous or not homogeneous lithology for FEM provides negligible
442 effects in stress intensity and pattern (Fig. 4). This is because the upper Units (*Units FC, VD, GF*;
443 Table 2) represent only a limited part of the simulated domain, which in the remaining part results
444 entirely composed of the assumed homogeneous basement (*Unit B*; Table 2). This does not mean that
445 the influence of the upper Units may be still negligible using smaller scales of the simulated domain.

446 Analysing the FEM outputs with the single magma chamber, it emerges how ΔP only limited the
447 effects of gravitational loading. The use of a dual magma chamber geometry better describes the
448 inflation induced by overpressure within magma chambers, with the formation of the stress arch in
449 the minimum compressive stress σ_3 plot.

450 It is important to highlight that for both single and dual magma chamber models, the change of
451 internal overpressure from 10 to 20 MPa slightly changes the magnitude of the stress but not their



452 general patterns (Appendix 1-2).

453 The presence of conduits in the magma feeding system dramatically change the σ_3 and σ_1 patterns
454 (Fig. 6). Indeed, they become quite homogeneous throughout the computational domain, with the
455 only exception of sidewall effects induced by the zero displacement conditions, already discussed in
456 Figure 4.

457 The addition of extensional field stress of 5 MPa reduces the sidewall effects and produces an almost
458 homogeneous stress distribution in the upper part of the FEM domain, above the top of the deep
459 magma chamber. This describes a close to equilibrium volcanic system, in which volcanic
460 overpressure and lithostatic stress almost equilibrate each other (Sulpizio et al., 2016).

461

462 *6.2 Some implication of the stress state of the CVC inferred from FEM*

463 The results obtained with the insertion of the full feeding system and far field stress on the FEM
464 highlight an almost homogeneous stress distribution in the CVC area. This means that the shape of
465 the dual magma chamber model plus conduits and far field stress provides a stable geometry, which
466 limits the stress changes to few MPa. All the large stress variations are located at the tips of the
467 magma chambers, as expected for pressurized or under-pressurized cavities in the lithosphere (Martì
468 and Geyer, 2009). This means that the whole feeding system is in a quasi-equilibrium state, and, as
469 an example, any overpressure created by input of new magma is adjusted by increasing the magma
470 chamber volume or erupting at the surface. Even if we consider the scenario of complete emptying
471 the upper conduit and part of the shallow magma chamber, as occasionally occurred in the past
472 originating sub-Plinian and Plinian eruptions (Luhr et al., 2002; Saucedo et al., 2010; Massaro et al.,
473 2018), this would result in the restoration of the stress arch, which is still a stable stress configuration.
474 Even the complete emptying of the shallow magma chamber probably would be ineffective for
475 triggering a large collapse (caldera forming) of the feeding system. This latter event would be
476 possible only if a large depressurization of the deeper magma chamber would occur, but it implies the
477 eruption of tens to hundreds of km³ of magma, which seems not very likely provided the current
478 stress distribution in CVC.

479 Beside and beyond the inaccuracies due to the first order approximation of the FEM analysis, other
480 sources of uncertainties in the discussion about present and future stress state of the CVC come from



481 the not consideration of gravity-driven processes as volcano spreading triggered by plastic
482 deformation of the GF Unit (Norini et al., 2010, 2019) or pressurization of the upper conduit
483 (Massaro et al., 2018), and detailed regional tectonics (Norini et al., 2010, 2019). Two main fault
484 systems have been described in the CVC and surrounding area: the N-S trending Colima Rift and a
485 set of E-W-trending faults (Fig. 1; Garduño-Monroy et al. 1998; Norini et al., 2010, 2019). The effect
486 on stress distribution of these regional fault systems are not included in the presented analysis, and
487 may alter significantly the stress patterns at a local scale, favouring intrusion of dykes or acting as
488 trigger of depressurization of the feeding system promoting eruptions or causing catastrophic
489 collapse of the upper edifice (e.g. Roverato et al., 2011).

490

491 **7 Conclusions**

492 The increasing detail of geological and geophysical data to FEM simulation at Colima Volcanic
493 Complex (Mexico) showed the importance of using the most accurate input data in order to have
494 reliable outputs. In particular, the data here presented highlighted how the use of simplified models
495 produces unreliable outputs of the stress state of the volcano subsurface.

496 Beside and beyond the results obtained by analysing the influence of detailing geological and
497 geophysical data, the FEM of CVC confirms the close to equilibrium state of the volcano, which is
498 the expected stress distribution induced by a feeding system directly connected to the surface.

499 This means that any overpressure created by input of new magma is adjusted within the feeding
500 system, sometimes triggering eruptions. The complete emptying the upper conduit and part of the
501 shallow magma chamber, as occasionally occurred in the past originating sub-Plinian and Plinian
502 eruptions would result in the restoration of the stress arch, which is still a stable stress configuration.
503 Descends that large magnitude, caldera forming eruptions are possible only if the deeper magma
504 chamber is involved and significantly emptied during an eruption.

505

506

507



508 **Appendices**

509

510 **Appendix 1**

511 E-W gravitational modelling of the CVC domain (stratified lithology) for all configurations
512 investigated. The magnitude and pattern of the principal stress account for a) single magma chamber
513 model; b) dual magma chamber model; c) dual magma chamber with conduits model (deep magma
514 chamber, $2a = 14$ km and $2b = 3.6$ km at 15 km of depth; shallow magma chamber, $2a = 3.5$ km and
515 $2b = 2$ km at 6 km. The magmatic overpressure is 20 MPa for the deep chamber, and 5 MPa for the
516 shallower.

517 **Appendix 2**

518 E-W gravitational modelling of the CVC domain (stratified lithology) considering a far extensional
519 stress field of 5 MPa for all configurations investigated. The magnitude and pattern of the principal
520 stress account for a) single magma chamber model; b) dual magma chamber model; c) dual magma
521 chamber with conduits model (deep magma chamber, $2a = 14$ km and $2b = 3.6$ km at 15 km of depth;
522 shallow magma chamber, $2a = 3.5$ km and $2b = 2$ km at 6 km. The magmatic overpressure is 20 MPa
523 for the deep chamber, and 5 MPa for the shallower.

524 **Code/Data Availability**

525 The LISA code is available at <https://lisafea.com/>.

526

527 **Author's contribution**

528 SM and RS wrote the manuscript with the input of all the co-authors. SM and GL compiled the
529 numerical simulations and formulated the adopted methodology. MP and SM carried out the
530 sensitivity analysis. RS, AC, SM, GN, GG, LC, GL, MP and AG worked on the interpretation of the
531 results.

532

533 **Competing interests:** The authors declare that they have no conflict of interest.

534 **Acknowledgements:** SM thanks the LISA customer service for the support received.



535 **References**

- 536 Anderson E.M., 1936. The dynamics of formation of cone sheets, ring dykes and cauldron subsidence.
537 Proc R Soc Edinburgh 56:128–163.
538
- 539 Allan, J.F., 1985. Sediment depth in the NCG from 3-D interpretation of gravity. *Geofis. Int.* 24, 21–
540 30 (1985).
- 541 Allan, J.F. 1986. Geology of the Northern Colima and Zacoalco grabens, Southwest Mexico: Late
542 Cenozoic rifting in the Mexican Volcanic Belt. *Geol. Soc. Am. Bull.* 97, 473–485
- 543 Allan, J.F., Nelson, S.A., Luhr, J.F., Charnichael, I.S.E., Wopat, M., Wallace, P.J., 1991: Pliocene-
544 Holocene rifting and associated volcanism in Southwest Mexico: an exotic terrane in the making. In:
545 Dauphin, J.P., Simoneit, R.R.T. (eds.) *The Gulf and Peninsular Provinces of the Californias*, AAPG
546 Mem., vol. 47, pp. 425–445
- 547 Andrew, R.E., and Gudmundsson, A., 2008. Volcanoes as elastic inclusions: Their effects on the
548 propagation of dykes, volcanic fissures, and volcanic zones in Iceland. *Journal of Volcanology and*
549 *Geothermal Research*, 177(4), 1045-1054.
550
- 551 Arámbula-Mendoza, R., Reyes-Dávila, G., Dulce, M.V.B., González-Amezcuca, M., Navarro- Ochoa,
552 C., Martínez-Fierros, A., and Ramírez-Vázquez, A., 2018. Seismic monitoring of effusive-explosive
553 activity and large lava dome collapses during 2013–2015 at Volcán de Colima, Mexico. *J. Volcanol.*
554 *Geotherm. Res.*, 351, 75-88.
- 555 Babuška, I., Ihlenburg, F., Paik, E. T., & Sauter, S.A., 1995. A generalized finite element method for
556 solving the Helmholtz equation in two dimensions with minimal pollution. *Computer methods in*
557 *applied mechanics and engineering*, 128(3-4), 325-359.
558
- 559 Bandy, W.L., Mortera-Gutiérrez, C.A., Urrutia- Fucugauchi, J., Hilde, T.W.C, 1995. The subducted
560 Rivera-Cocos plate boundary: where is it, what is it, and what is its relationship to the Colima Rift?
561 *Geophys. Res. Lett.* 22, 3075–3078.
- 562 Barrier, B., Bourgois, J., Michaud, F., 1990: The active Jalisco triple junction rift system. *C.R. Acad.*
563 *Sci. Paris*, 310 (II), 1513–1520.
- 564 Bathe, K. J., Zhang, H., & Ji, S., 1999. Finite element analysis of fluid flows fully coupled with
565 structural interactions. *Computers & Structures*, 72(1-3), 1-16.
566
- 567 Bonafede, M., Parenti, B., Rivalta, E., 2002. On strike-slip faulting in layered media. *Geophysical*
568 *Journal International*, 149(3), 698-723.
569
- 570 Bonasia R, Capra L, Costa A, Macedonio G, Saucedo R., 2011. Tephra fallout hazard assessment for
571 a Plinian eruption scenario at Volcan de Colima. *J Volcanol Geotherm Res* 203: 12–22.
572
- 573 Boresi, A.P., Schmidt, R.J., & Sidebottom, O.M., 1985. *Advanced mechanics of materials* (Vol. 6).
574 New York et al.: Wiley.
575
- 576 Buchmann T. and Conolly P.T., 2007. Contemporary kinematics of the Upper Rhine Graben: A 3D
577 finite element approach. *Global and Planetary Change* 58, 287–309.
- 578 Bunney, 2014. *The Effects of Structural Heterogeneities and In-elastic Rheology on Ground*
579 *Deformation at Campi Flegrei Caldera, Italy*. PhD Thesis.
- 580
- 581 Cabaniss, H.E., Gregg, P. M., & Grosfils, E.B., 2018. The role of tectonic stress in triggering large
582 silicic caldera eruptions. *Geophysical Research Letters*, 45, 3889–3895. [https://doi.org/10.1029/](https://doi.org/10.1029/2018GL077393)
583 [2018GL077393](https://doi.org/10.1029/2018GL077393) .



- 584 Beatrice Cailleau, Thomas R. Walter, Peter Janle, Ernst Hauber, 2005. Unveiling the origin of radial
585 grabens on Alba Patera volcano by finite element modelling *Icarus* 176, 44–56.
586
- 587 Cailleau, B., T.R. Walter, P. Janle, and E. Hauber, 2003. Modeling volcanic deformation in a regional
588 stress field: Implications for the formation of graben structures on Alba Patera, Mars, *J. Geophys.*
589 *Res.*, 108(E12), 5141, doi:10.1029/2003JE002135.
- 590
- 591 Cabrera-Gutiérrez, R., and Espíndola, J.M., 2010. The 1998-1999 eruption of Volcán de Colima,
592 Mexico: an application of Maeda's viscoelastic model. *Geofísica internacional*, 49(2), 83-96.
593
- 594 Canales, J. P., Nedimović, M. R., Kent, G.M., Carbotte, S.M., & Detrick, R.S., 2009. Seismic
595 reflection images of a near-axis melt sill within the lower crust at the Juan de Fuca ridge. *Nature*,
596 460(7251), 89.
597
- 598 Capra, L., & Macías, J.L., 2002. The cohesive Naranjo debris-flow deposit (10 km³): A dam breakout
599 flow derived from the Pleistocene debris-avalanche deposit of Nevado de Colima Volcano (México).
600 *Journal of Volcanology and Geothermal Research*, 117(1-2), 213-235.
601
- 602 Capra L, Macías JL, Cortés A, Dávila N, Saucedo R, Osorio-Ocampo S, Arce JL, Galvilanes-Ruiz JC,
603 Corona-Càvez P, García-Sánchez L, Sosa-Ceballos G, Vasquez R., 2016. Preliminary report on the
604 July 10–11, 2015 eruption at Volcán de Colima: Pyroclastic density currents with exceptional runouts
605 and volume, *J Volcanol Geotherm Res* 310: 39-49.
606
- 607 Charco, M., & Galán del Sastre, P., 2014. Efficient inversion of three-dimensional finite element
608 models of volcano deformation. *Geophysical Journal International*, 196(3), 1441-1454.
609
- 610 Chen, H.X., Hong H.J., Liu H., 2009. Volcano-tectonic interaction and its relation with the state of
611 volcanic activity. *Chinese Journal of Geophysics*. Vol. 52, n.3, pp. 596-603.
612
- 613 Cortés, A., 2005. Carta geológica del complejo volcánico de Colima. UNAM, Instituto de Geología.
614
- 615 Cortes A, Macías JL, Capra L and Garduño-Monroy V.H., 2010. Sector collapse of the SW flank of
616 Volcán de Colima, México. The 3600 yr BP La Lumbre-Los Ganchos debris avalanche and
617 associated debris flows. *J Volcanol Geotherm Res* 197: 52-66.
618
- 619 Costa, A., Sparks, R. S. J., Macedonio, G., & Melnik, O., 2009. Effects of wall-rock elasticity on
620 magma flow in dykes during explosive eruptions. *Earth and Planetary Science Letters*, 288(3-4), 455-
621 462.
622
- 623 Costa, A., Gottsmann, J., Melnik, O., & Sparks, R. S. J., 2011. A stress-controlled mechanism for the
624 intensity of very large magnitude explosive eruptions. *Earth and Planetary Science Letters*, 310(1-2),
625 161-166.
626
- 627 Corbi, F., Rivalta, E., Pinel, V., Maccaferri, F., Bagnardi, M., & Acocella, V., 2015. How caldera
628 collapse shapes the shallow emplacement and transfer of magma in active volcanoes. *Earth and*
629 *Planetary Science Letters*, 431, 287-293.
630
- 631 Currenti, G., Bonaccorso, A., Del Negro, C., Scandura, D., & Boschi, E., 2010. Elasto-plastic
632 modeling of volcano ground deformation. *Earth and Planetary Science Letters*, 296(3-4), 311-318.
633
- 634 Currenti, G., and Williams, C.A., 2014. Numerical modeling of deformation and stress fields around
635 a magma chamber: Constraints on failure conditions and rheology. *Physics of the Earth and Planetary*
636 *Interiors*, 226, 14-27.
637
- 638 Dávila, N., Capra, L., Ferrés, D., Gavilanes-Ruiz, J. C., & Flores, P., 2019. Chronology of the 2014–
639 2016 Eruptive Phase of Volcán de Colima and Volume Estimation of Associated Lava Flows and
640 Pyroclastic Flows Based on Optical Multi-Sensors. *Remote Sensing*, 11(10), 1167.
641



- 642
643 Del Potro, R., Hürlimann, M., 2008. Geotechnical classification and characterization of materials for
644 stability analyses of large volcanic slopes. *Eng. Geol.* 98(1), 1–17.
- 645 Dieterich J.H., and R.W. Decker, 1975. Finite element modeling of surface deformation associated
646 with volcanism, *J. Geophys. Res.*, 80, 4094–4102.
- 647 Duvinage, I., Mallet, J.L., Dulac, J.C., 1999. Extracting information from faulted horizon boundaries
648 for building and updating of a 3D model. In: American Association of Petroleum Geologists, Annual
649 Meeting Expanded Abstracts.
- 650 Escudero, C.R., Bandy, W.L., 2017: Ambient seismic noise tomography of the Colima Volcano
651 Complex. *Bull. Volcanol.* 79, 13.
- 652 Fernández, J., Tiampo, K. F., Jentzsch, G., Charco, M., & Rundle, J.B., 2001. Inflation or deflation?
653 New results for Mayon Volcano applying elastic - gravitational modeling. *Geophysical Research*
654 *Letters*, 28(12), 2349-2352.
- 655
656 Ferrari, L., Rosas-Elguera, J., Márquez, A., Oyarzun, R., Doblas, M., & Verma, S.P., 1999. Alkalic
657 (ocean-island basalt type) and calc-alkalic volcanism in the Mexican volcanic belt: A case for plume-
658 related magmatism and propagating rifting at an active margin?: Comment and Reply. *Geology*,
659 27(11), 1055-1056.
- 660
661 Folch, A., Fernández, J., Rundle, J.B., Martí, J., 2000. Ground deformation in a viscoelastic medium
662 composed of a layer overlying a half-space: a comparison between point and extended sources.
663 *Geophys. J. Int.* 140 (1), 37–50.
- 664 Frey, H.M., Lange, R.A., Hall, C.M., Delgado-Granados, H., Carmichael, I.S.E., 2007. A Pliocene
665 ignimbrite flare-up along the Tepic-Zacoalco rift: evidence for the initial stages of rifting between the
666 Jalisco block (Mexico) and North America. *Geol. Soc. Am. Bull.* 119, 49–64.
667 <http://dx.doi.org/10.1130/B25950.1>.
- 668 Fujita, E., Kozono, T., Ueda, H., Kohno, Y., Yoshioka, S., Toda, N., ... & Ida, Y., 2013. Stress field
669 change around the Mount Fuji volcano magma system caused by the Tohoku megathrust earthquake,
670 *Japan. Bulletin of volcanology*, 75(1), 679.
- 671
672 Gabrieli, A., Wilson, L., and Lane, S., 2015. Volcano–tectonic interactions as triggers of volcanic
673 eruptions. *Proceedings of the Geologists' Association*, 126(6), 675-682.
- 674
675 Garduño-Monroy, V.H., Saucedo-Girón, R., Jiménez, Z., Gavilanes-Ruiz, J.C., Cortés-Cortés, A.,
676 Uribe-Cifuentes, R.M. 1998: La Falla Tamazula, límite suroriental del Bloque Jalisco, y sus
677 relaciones con el Complejo Volcánico de Colima, México. *Revista Mexicana de Ciencias Geológicas*
678 15(2), 132–144.
- 679
680 Geyer, A., and Gottsmann, J., 2010. The influence of mechanical stiffness on caldera deformation
681 and implications for the 1971–1984 Rabaul uplift (Papua New Guinea). *Tectonophysics*, 483(3-4),
682 399-412.
- 683 Gerbault, M., Cappa, F., Hassani, R., 2012. Elasto-plastic and hydromechanical models of failure
684 around an infinitely long magma chamber. *Geochem. Geophys. Geosyst.* 13, Q03009.
685 <http://dx.doi.org/10.1029/2011GC003917>.
- 686
687 Gerbault, M., Hassani, R., Lizama CN, Souche, A., 2018. Three-Dimensional Failure Patterns Around
688 an Inflating Magmatic Chamber. *Geochemistry, Geophysics, Geosystems*, AGU and the
Geochemical Society, In press.
- 689
690 Geshi, N., Kusumoto, S., & Gudmundsson, A., 2012. Effects of mechanical layering of host rocks on
691 dike growth and arrest. *Journal of Volcanology and Geothermal Research*, 223, 74-82.



- 692 Gottsmann, J., Folch, A., & Rymer, H., 2006. Unrest at Campi Flegrei: A contribution to the
693 magmatic versus hydrothermal debate from inverse and finite element modeling. *Journal of*
694 *Geophysical Research: Solid Earth*, 111(B7).
695
- 696 Grosfils, E.B., 2007. Magma reservoir failure on the terres- trial planets: Assessing the importance of
697 gravitational loading in simple elastic models, *J. Volcanol. Geotherm. Res.*, 166, 47–75,
698 doi:10.1016/j.jvolgeores.2007.06.007.
- 699 Grosfils, E.B., McGovern, P. J., Gregg, P.M., Galgana, G.A., Hurwitz, D.M., Long, S.M., Chestler,
700 S.R., 2015. Elastic models of magma reservoir mechanics: a key tool for investigating planetary
701 volcanism. *Geol. Soc. London, Spec. Pub.*, 401(1), 239-267.
- 702 Gudmundsson, A., and Brenner, S.L., 2004. How mechanical layering affects local stresses, unrests,
703 and eruptions of volcanoes. *Geophysical Research Letters*, 31(16).
704
- 705 Gudmundsson, A., 2006. How local stresses control magma-chamber ruptures, dyke injections, and
706 eruptions in composite volcanoes, *Earth-Sci.Rev.*, 79(1–2), 1–31.
- 707 Goennermann and Taisne, 2015. Magma Transport in Dikes. *The Encyclopedia of Volcanoes*.
708 <http://dx.doi.org/10.1016/B978-0-12-385938-9.00010-9>
- 709 Hautmann, S., Gottsmann, J., Sparks, R. S. J., Costa, A., Melnik, O., & Voight, B., 2009. Modelling
710 ground deformation caused by oscillating overpressure in a dyke conduit at Soufrière Hills Volcano,
711 Montserrat. *Tectonophysics*, 471(1-2), 87-95.
- 712 Hickey, J., Gottsmann, J., and Mothes, P., 2015. Estimating volcanic deformation source
713 parameters with a finite element inversion: The 2001–2002 unrest at Cotopaxi volcano, Ecuador, *J.*
714 *Geophys. Res. Solid Earth*, 120, 1473–1486, doi:10.1002/2014JB011731.
- 715 Hoek, E., Brown, E.T, 1997. Practical estimates of rock mass strength. *Int. J. Rock Mech. Min. Sci.*
716 34, 1165–1186.
- 717 Holohan, E. P., T. R. Walter, M. P. J. Schopfer, J. J. Walsh, B. van Wyk de Vries, and V. R. Troll,
718 2013. Origins of oblique-slip faulting during caldera subsidence, *J. Geophys. Res. Solid Earth*, 118,
719 1778–1794, doi:10.1002/jgrb.50057.
- 720 Huang, X., & Zhang, Z., 2012. Stress arch bunch and its formation mechanism in blocky stratified
721 rock masses. *Journal of Rock Mechanics and Geotechnical Engineering*, 4(1), 19-27.
722
- 723 Karlstrom, L., Dufek, J., Manga, M., 2010. Magma chamber stability in arc and continental crust. *J.*
724 *Volcanol. Geotherm. Res.* 190, 249–270.
725
- 726 Jellinek, A.M., DePaolo, D.J., 2003. A model for the origin of large silicic magma chambers:
727 precursors of caldera-forming eruptions. *Bull. Volcanol.* 65, 363–381.
728
- 729 Lister, J.R., Kerr, R.C., 1991. Fluid-mechanical models of crack propagation and their application to
730 magma transport in dykes. *Journal of Geophysical Research* 96,10,049–10,077.
- 731 Long, S.M., and Grosfils, E.B., 2009. Modeling the effect of layered volcanic material on magma
732 reservoir failure and associated deformation, with application to Long Valley caldera, California.
733 *Journal of Volcanology and Geothermal Research*, 186(3-4), 349-360.
734
- 735 López-Loera, H., Urrutia-Fucugauchi, J., Alva-Valdivia, L., 2011. Estudio aeromagnético del
736 complejo volcánico de Colima, occidente de México – implicaciones tectónicas y estructurales.
737 *Revista Mexicana de Ciencias Geológicas* 28, 349–370.
- 738 Lungarini, L., Troise, C., Meo, M., & De Natale, G., 2005. Finite element modelling of topographic
739 effects on elastic ground deformation at Mt. Etna. *Journal of volcanology and geothermal research*,
740 144(1-4), 257-271.



- 741 Luhr, J.F., and Carmichael, I.S., 1985. Contemporaneous eruptions of calc-alkaline and alkaline
742 magmas along the volcanic front of the Mexican Volcanic Belt. *Geofísica Internacional*, 24(1).
743
- 744 Luhr, J.F., & Prestegard, K.L., 1988. Caldera formation at Volcán Colima, Mexico, by a large
745 holocene volcanic debris avalanche. *Journal of Volcanology and Geothermal Research*, 35(4), 335-
746 348.
747
- 748 Luhr JF., 2002. Petrology and geochemistry of the 1991 and 1998-1999 lava flows from Volcan
749 Colima, Mexico. *J Volcanol Geotherm Res* 117: 169–194.
750
- 751 Komorowski, J. C., Navarro, C., Cortes, A., Saucedo, R., Gavilanes, J. C., Siebe, C., ... & Rodriguez-
752 Elizarrarás, S. R., 1997. The Colima Volcanic Complex. Field guide, 3.
753
- 754 Maccaferri, F., Bonafede, M., & Rivalta, E., 2010. A numerical model of dyke propagation in layered
755 elastic media. *Geophysical Journal International*, 180(3), 1107-1123.
756
- 757 Maccaferri, F., Rivalta, E., Keir, D., & Acocella, V., 2014. Off-rift volcanism in rift zones
758 determined by crustal unloading. *Nature Geoscience*, 7(4), 297-300.
759
- 760 Macías, J.L., Saucedo, R., Gavilanes, J.C., Varley, N., Velasco, García S., Bursik, M.I., Vargas,
761 Gutiérrez V., Cortés, A., 2006. Flujos piroclásticos asociados a la activi- dad explosiva del Volcán de
762 Colima y perspectivas futuras. *GEOS* 25(3), 340–351.
- 763 Macías J, Arce J, Sosa G, Gardner JE, Saucedo R., 2017. Storage conditions and magma processes
764 triggering the 1818CE Plinian eruption of Volcán de Colima. *J Volcanol GeothermRes*
765 doi:10.1016/j.jvolgeores.2017.02.025.
- 766 Macdonald, K.C., 1982. Mid-ocean ridges: fine scale tectonic, volcanic and hydrothermal pro-
767 cesses within the plate boundary zone. *Annual Review of Earth and Planetary Sciences* 10, 155–190.
- 768 MacLeod, C.J., Yaouancq, G., 2000. A fossil melt lens in the Oman ophiolite: implications for
769 magma chamber processes at fast spreading ridges. *Earth and Planetary Science Letters* 176, 357–373.
- 770 Mallet, J.L., 2002. *Geomodeling*. Oxford University Press.
- 771 Mallet, J.L., 1989. Discrete smooth interpolation in geometric modeling. *Comput. Aided Des.* 24 (4),
772 177–191.
- 773 Manconi A., Walter TR, and Amelung, F., 2007. Effects of mechanical layering on volcano
774 deformation. *Geophys. J. Int.* (2007) 170, 952–958.
- 775 Manconi, A., Longpré, M.A., Walter, T.R., Troll, V.R., Hansteen, T.H., 2009. The effects of flank
776 collapses on volcano plumbing systems. *Geology* 37 (12), 1099–1102.
- 777 Marinos, P., Hoek, E., 2000. GSI: a geologically friendly tool for rock mass strength estimation. In:
778 *Proc. GeoEng2000 Conference*, Melbourne, 1422–1442.
- 779 Martí, J., & Geyer, A., 2009. Central vs flank eruptions at Teide–Pico Viejo twin stratovolcanoes
780 (Tenerife, Canary Islands). *Journal of Volcanology and Geothermal Research*, 181(1-2), 47-60.
781
- 782 Massaro, S., Costa, A., Sulpizio, R., Coppola, D., Capra, L., 2019. Cyclic activity of Fuego de
783 Colima volcano (Mexico): insights from satellite thermal data and non-linear models. In press, *Solid*
784 *Earth*.
- 785 Massaro S, Sulpizio R, Costa A, Capra L., Lucchi F., 2018. Understanding eruptive style variations at
786 calc-alkaline volcanoes: the 1913 eruption of Fuego de Colima volcano (Mexico). *Bulletin of*
787 *Volcanology*, 80:62.



- 788 Sulpizio, R., & Massaro, S., 2017. Influence of stress field changes on eruption initiation and
789 dynamics: a review. *Frontiers in Earth Science*, 5, 18.
790
- 791 Masterlark, T., Feigl, K. L., Haney, M., Stone, J., Thurber, C., & Ronchin, E., 2012. Nonlinear
792 estimation of geometric parameters in FEMs of volcano deformation: Integrating tomography models
793 and geodetic data for Okmok volcano, Alaska. *Journal of Geophysical Research: Solid Earth*,
794 117(B2).
795
- 796 Medina-Martínez, F., Espíndola, J.M., De la Fuente, M., Mena, M., 1996. A gravity model of the
797 Colima, México region. *Geofis. Int.* 35(4), 409–414.
- 798 Michaeli, W., 1991. *Extrusionswerkzeuge für Kunststoffe und Kautschuk: Bauarten, Gestaltung und*
799 *Berechnungsmöglichkeiten.* Hanser Verlag.
800
- 801 Moeck, I., Schandelmeier, H. & Holl, HG., 2009. The stress regime in a Rotliegend reservoir of the
802 Northeast German Basin. *Int. J. Earth. Sci.* 98, 1643-1654.
- 803 Mutter, J.C., Carbotte, S.M., Su, W.S., Xu, L.Q., Buhl, P., Detrick, R.S., Kent, G.M., Orcutt, J.A.,
804 Harding, A.J., 1995. Seismic images of active magma systems beneath the East Pacific Rise between
805 17-degrees-05's and 17-degrees-35's. *Science* 268, 391–395.
- 806 Newman, A. V., Dixon, T. H., Ofoegbu, G. I., & Dixon, J. E., 2001. Geodetic and seismic constraints
807 on recent activity at Long Valley Caldera, California: evidence for viscoelastic rheology. *Journal of*
808 *Volcanology and Geothermal Research*, 105(3), 183-206.
809
- 810 Norini, G., Agliardi, F., Crosta, G., Groppelli, G., & Zuluaga, M.C., 2019. Structure of the Colima
811 Volcanic Complex: Origin and Behaviour of Active Fault Systems in the Edifice. In *Volcán de*
812 *Colima* (pp. 27-54). Springer, Berlin, Heidelberg.
813
- 814 Norini G, Capra L, Groppelli G, Agliardi F, Pola A, Cortes A., 2010. Structural architecture of the
815 Colima Volcanic Complex. *J Geophys Res* 115, B12209.
816
- 817 Núñez-Cornú F, Nava FA, De la Cruz-Reyna S, Jiménez Z, Valencia C, García-Arthur R., 1994.
818 Seismic activity related to the 1991 eruption of Colima Volcano, Mexico. *Bull Volcanol* 56: 228–237.
819
- 820 Parfitt, E. A., and L. Wilson, 2008. "The role of volatiles." *Fundamentals of Physical Volcanology*,
821 64-76.
822
- 823 Pinel, V., & Jaupart, C., 2004. Magma storage and horizontal dyke injection beneath a volcanic
824 edifice. *Earth and Planetary Science Letters*, 221(1-4), 245-262.
825
- 826 Pritchard, M. E., & Simons, M., 2004. An InSAR-based survey of volcanic deformation in the central
827 Andes. *Geochemistry, Geophysics, Geosystems*, 5(2).
828
- 829 Rao SS., 1989. *The Finite Element Method in Engineering* second edition. PERGAMON PRESS
830 1989 ISBN 0-08-033419-9.
- 831 Rao, S.S., 2013. *The Finite Element Method in Engineering: Pergamon International Library of*
832 *Science, Technology, Engineering and Social Studies.* Elsevier.
833
- 834 Reubi, O., Blundy, J., & Varley, N.R., 2013. Volatiles contents, degassing and crystallisation of
835 intermediate magmas at Volcan de Colima, Mexico, inferred from melt inclusions. *Contributions to*
836 *Mineralogy and Petrology*, 165(6), 1087-1106.
837
- 838 Reubi, O., Blundy, J., & Pickles, J., 2019. Petrological monitoring of Volcán de Colima magmatic
839 system: the 1998 to 2011 activity. In *Volcán de Colima* (pp. 219-240). Springer, Berlin, Heidelberg.
840
- 841 Rivalta et al., 2019. Stress inversions to forecast magma pathways and eruptive vent location *Sci.*
842 *Adv.* 2019; 5:eaau9784 .



- 843 Robin, C., Mossand, P., Camus, G., Cantagrel, J. M., Gourgaud, A., & Vincent, P.M., 1987. Eruptive
844 history of the Colima volcanic complex (Mexico). *Journal of Volcanology and Geothermal*
845 *Research*, 31(1-2), 99-113.
846
- 847 Ronchin, E., Geyer, A., & Martí, J., 2015. Evaluating topographic effects on ground deformation:
848 insights from finite element modeling. *Surveys in Geophysics*, 36(4), 513-548.
849
- 850 Rosas-Elguera, J., Ferrari, L., Garduño-Monroy, V.H., Urrutia-Fucugauchi, J., 1996: Continental
851 boundaries of the Jalisco block and their influence in the Pliocene-Quaternary kinematics of western
852 Mexico. *Geology* 24, 921–924.
- 853 Rosas-Elguera J, Ferrari L, Martinez ML, Urrutia-Fucugauchi J., 1997. Stratigraphy and tectonics of
854 the Guadalajara region and triple- junction area, western Mexico. *Int Geol Rev* 39:125–140.
855 doi:10.1080/00206819709465263.
- 856 Rosas-Elguera, J., Alva-Valdivia, L. M., Goguitchaichvili, A., Urrutia-Fucugauchi, J., Ortega-Rivera,
857 M. A., Prieto, J.C.S., and Lee, J.K., 2003. Counterclockwise rotation of the Michoacan Block:
858 implications for the tectonics of western Mexico. *International Geology Review*, 45(9), 814-826.
859
- 860 Roverato, M., Capra, L., Sulpizio, R., Norini, G., 2011. Stratigraphic reconstruction of two debris
861 avalanche deposits at Colima Volcano (Mexico): insights into pre-failure conditions and climate
862 influence. *Journal of Volcanology and Geothermal Research*, 207(1-2), 33-46, 2011
- 863 Roverato, M., & Capra, L., 2013. Características microtexturales como indicadores del transporte y
864 emplazamiento de dos depósitos de avalancha de escombros del Volcán de Colima (México). *Revista*
865 *mexicana de ciencias geológicas*, 30(3), 512-525.
866
- 867 Salzer JT, Nikkhoo M, Walter T, Sudhaus H, Reyes-Dávila G, Bretòn-Gonzalez M, Aràmbula R.,
868 2014. Satellite radar data reveal short-term pre-explosive displacements and a complex conduit
869 system at Volcan de Colima, Mexico. *Front Earth Sci* 2:12.
870
- 871 Saada, A.S., 2009. *Elasticity: Theory and Applications*. Krieger, Malabar, Florida.
- 872 Savin, G. N., 1961. Stress concentration around holes.
873
- 874 Saucedo R, Macías J., Gavilanes JC, Arce JL, Komorowski JC, Gardner JE, Valdez-Moreno G
875 (2010) Eyewitness, stratigraphy, chemistry, and eruptive dynamics of the 1913 Plinian eruption of
876 Volcán de Colima. México. *J Volcanol Geotherm Res* 191:149–166.
877
- 878 Saucedo R, Macías JL, Gavilanes JC, Arce JL, Komorowski JC, Gardner JE, and Valdez-Moreno G.,
879 2011. Corrigendum to Eyewitness, stratigraphy, chemistry, and eruptive dynamics of the 1913
880 plinian eruption of Volcan de Colima, Mexico. *J Volcanol Geotherm Res* 191:149–166.
881
- 882 Schwarz, H.R., 1991. *Methode der finiten Elemente* neubearbeitete Auflage, B.G. Teubner Stuttgart
883 ISBN 3-519-22349-X.
- 884 Selvans, M. M., Stock, J. M., DeMets, C., Sanchez, O., & Marquez-Azua, B., 2011. Constraints on
885 Jalisco Block motion and tectonics of the Guadalajara triple junction from 1998–2001 Campaign
886 GPS Data. *Pure and applied geophysics*, 168(8-9), 1435-1447.
887
- 888 Serpa, L., Smith, S., Katz, C., Skidmore, C., Sloan, R., Pavlis, T., 1992. A geophysical investigation
889 of the southern Jalisco block in the state of Colima, Mexico. *Geofisica Internacional* 31, 247–252.
- 890 Simms MA., and Graven G., 2004. Thermal convection in faulted extensional sedimentary basins:
891 theoretical results from finite-element modelling. *Geofluids* (2004), 4, 109-130.
892
- 893 Singh, S. C., Crawford, W. C., Carton, H., Seher, T., Combier, V., Cannat, M., ... & Miranda, J. M.,
894 2006. Discovery of a magma chamber and faults beneath a Mid-Atlantic Ridge hydrothermal field.
895 *Nature*, 442(7106), 1029.



- 896 Sinton, J.M., and Detrick, R.S., 1992. Mid-ocean ridge magma chambers. *Journal of Geophysical*
897 *Research: Solid Earth*, 97(B1), 197-216.
898
- 899 Stock JM, Lee J., 1994. Do microplates in subduction zones leave a geological record? *Tectonics*
900 13:1472–1487.
- 901 Stoopes, G. R., & Sheridan, M.F., 1992. Giant debris avalanches from the Colima Volcanic Complex,
902 Mexico: Implications for long-runout landslides (> 100 km) and hazard assessment. *Geology*, 20(4),
903 299-302.
904
- 905 Spica, Z., Cruz-Atienza, V.M., Reyes-Alfaro, G., Legrand, D., and Iglesias, A., 2014. Crustal
906 imaging of western Michoacán and the Jalisco Block, Mexico, from ambient seismic noise. *Journal*
907 *of Volcanology and Geothermal Research*, 289, 193-201.
908
- 909 Spica Z, Perton M, Legrand D., 2017. Anatomy of the Colima volcano magmatic system,
910 Mexico, *Earth Planet Sci Lett* 459: 1-13.
911
- 912 Suárez, G., Garcia-Acosta, V., Gaulon, R., 1994. Active crustal deformation in the Jalisco block,
913 Mexico: evidence for a great historical earthquake in the 16th century. *Tectonophysics* 234, 117–12.
- 914 Sulpizio, R., Lucchi, F., Forni, F., Massaro, S., & Tranne, C., 2016. Unravelling the effusive-
915 explosive transitions and the construction of a volcanic cone from geological data: The example of
916 Monte dei Porri, Salina Island (Italy). *Journal of Volcanology and Geothermal Research*, 327, 1-22.
917
- 918 Tan, S.C., 1994. *Stress Concentrations in Laminated Composites*. Technomic, Basel.
- 919 Tibaldi, A., 2015. Structure of volcano plumbing systems: A review of multi-parametric effects.
920 *Journal of Volcanology and Geothermal Research* 298 (2015) 85–135.
- 921 Trasatti, E., Casu, F., Giunchi, C., Pepe, S., Solaro, G., Tagliaventi, S., ... & Sansosti, E., 2008. The
922 2004–2006 uplift episode at Campi Flegrei caldera (Italy): Constraints from SBAS-DInSAR
923 ENVISAT data and Bayesian source inference. *Geophysical Research Letters*, 35(7).
924
- 925 Turcotte, D. L. & Schubert, G., 2002. *Geodynamics*, 2nd edition, Cambridge University Press.
- 926 Zehner B, Jana H. Börner JH, Görz I , Spitzer K., 2015. Workflows for generating tetrahedral meshes
927 for finite element simulations on complex geological structures. *Computers and Geosciences*, 79,
928 105-117.
- 929 Zhao, S., Muller, R. D., Takahashi, Y. & Kaneda, Y., 2004. 3-D finite-element modelling of
930 deformation and stress associated with faulting: effect of inhomogeneous crustal structures, *Geophys.*
931 *J. Int.*, 157, 629– 644.
- 932 Zhong, X. Marcin, Dabrowski, Bjørn Jamtveit, 2019. Analytical solution for the stress field in elastic
933 half space with a spherical pressurized cavity or inclusion containing eigenstrain. *Geophysical*
934 *Journal International* · (submitted).
- 935 Zobin, V.M., Luhr, J.F., Taran, Y.A., Bretón, M., Cortés,A., De la Cruz-Reyna, S., Domínguez, T.,
936 Galindo, I., Gavilanes, J.C., Muñiz, J.J., Navarro, C., Ramírez, J. J., Reyes, G.A., Ursúa, M., Velasco,
937 J., Alatorre, E., Santiago, H., 2002. Overview of the 1997–2000 activity of Volcán de Colima,
938 Mexico. *J. Volcanol. Geotherm.Res.* 117, 1–19.
939
- 940 Watanabe, T., Masuyama, T., Nagaoka, K., Tahara, T., 2002. Analog experiments on magma-filled
941 cracks: competition between external stresses and internal pressure. *Earth Planets Space* 54, 1247–
942 1261.
- 943 Wang, R., Martin, F.L. & Roth, F., 2003. Computation of deformation induced by earthquakes in a
944 multi-layered elastic crust-FORTRAN programs EDGRN/EDCMP, *Comput. Geosci.*, 29, 195–207.
945



946 Weiler, K., 1988. The radial edge structure: a topological representation for non- manifold geometric
 947 boundary modeling In: Wozny, M., McLaughlin, H., Encarna (Eds.), Geometric Modeling for CAD
 948 Application. Elsevier, Amsterdam, 3–36.

949

950 **Table 1** - Input parameters used in finite-element model.

951

Element types used in LISA analysis.

<i>E-W cross-section (a-a')</i>		Element Type	Quantity
FC	Fuego de Colima	quad4	596
VD	Volcanic Deposits	quad4	235
GF	Graben Fill	quad4	434
B	Basament	quad4	3395

Total Elements: 4660

952 **Table 2** - Rock mass and mechanical properties used in the finite-element model (from Norini et al.
 953 2010; 2019).

954

Acronym	Model Unit	Rock Type	Density (kg/m ³)	Young's Modulus (MPa)	Poisson's ratio ν
<i>FC</i>	Fuego de Colima	Andesitic lavas and pyroclastic deposits forming the Paleofuego-Fuego de Colima volcano	2242	1.4×10^3	0.30
<i>VD</i>	Volcaniclastic deposits	Pyroclastic and epiclastic deposits covering the southern flank of the CVC	1539	1.7×10^3	0.32
<i>GF</i>	Graben Fill	Quaternary alluvial, colluvial, lacustrine deposits filling the graben	1834	1.5×10^3	0.35
<i>B</i>	Basement	Cretaceous limestones and intrusive rocks forming the bed-rock underlying the CVC	2650	3.6×10^4	0.30

955

956

957



958 **Figures Captions**

959

960 **Fig. 1** (a) Morphotectonic map of the Colima Volcanic Complex (NC=Nevado de Colima volcano;
961 FC=Fuego de Colima volcano) and Colima Rift with the main tectonic and volcano-tectonic
962 structures (NCG =Northern Colima Graben; CCG= Central Colima Graben, from Norini et al., 2019).
963 In the inset, the location of the Colima Volcanic Complex (CVC) within the Trans-Mexican Volcanic
964 Belt (TMVB) is shown in the frame of the subduction-type geodynamic setting of Central America
965 (from Davila et al., 2019); (b) general sketch of the geometrical configurations used in FE modelling
966 for the E-W cross-section.

967

968 **Fig. 2** Sensitivity analysis of the Young's Modulus variations within the investigated domain
969 configurations (stratified substratum model, single magma chamber model, dual magma chamber
970 model, and dual magma chamber with conduits model). For each Units (*B*, *FC*, *GF*, *VD*), the *relative*
971 *global variation in L2* is provided for σ_1 and σ_3 . The $x(-)$ and $x(+)$ vectors indicate the Young
972 Modulus variation by an order of magnitude with respect to x_{ref} vector, containing the stress values
973 calculated by using the values of material's properties indicated in Table 2.

974

975 **Fig. 3** Spatial variation of the L_2 norm's components at varying Young Modulus in *Units B* for the
976 stratified substratum (a), the single (b) and dual (c) magma chamber models, and in *Units VD* for the
977 dual magma chamber with conduits model (d).

978

979 **Fig. 4** E-W gravitational modelling of the CVC domain. The scale of the mesh is expressed in Unit
980 of Design (1 UD = 1 km). The domain extends 60 km along the x -axis, and 30 km along the z -axis.
981 The magnitude and pattern of the principal stresses (dotted black lines) are reported for a
982 homogeneous lithology (HL: *Unit FC* =andesitic lavas and pyroclastic deposits) and for a stratified
983 lithology (SL: *Unit B*= Cretaceous limestones and intrusive rocks forming the bed-rock underlying
984 the CVC; *Unit GF*=Quaternary alluvial, colluvial, and lacustrine deposits filling the graben; *Unit FC*;
985 *Unit VD*= volcanoclastic deposits covering the southern flank of the CVC). The blue contour defines
986 the unperturbed part of the domain, which extends ca. 30 km horizontally and ca. 15 km vertically.

987

988

989 **Fig. 5** E-W gravitational modelling of the CVC domain (stratified lithology). The magnitude and
990 pattern of the principal stresses are reported for (a) the single magma chamber model represented by
991 a deep magma chamber ($2a = 14$ km and $2b = 3.6$ km) at 15 km of depth, and for (b) the dual magma
992 chamber model composed of a 15-km deep ($2a = 14$ km and $2b = 3.6$ km) and 6-km deep ($2a = 3.5$



993 km and $2b = 2$ km) magma chambers. These chambers are not connected via dykes. The magmatic
994 overpressure is 10 MPa for the deep magma chambers (a,b) and 5 MPa for the shallow one (b).

995 **Fig. 6** E-W gravitational modelling of the CVC domain (stratified lithology). The magnitude and
996 pattern of the principal stresses account for a dual magma chamber system connected by dykes via
997 surface (deep magma chamber, $2a = 14$ km and $2b = 3.6$ km at 15 km of depth; shallow magma
998 chamber, $2a = 3.5$ km and $2b = 2$ km at 6 km). The magmatic overpressure is 10 MPa for the deep
999 chamber, 5 MPa for the shallow one.

.000

.001 **Fig. 7** E-W gravitational modelling of the CVC domain (stratified lithology) when considering an
.002 extensional stress field of 5 MPa. The magnitude and pattern of the principal stresses are shown for i-
.003 ii) the single magma chamber model, iii-vi) the dual magma chamber model, and v-vi) the dual
.004 magma chamber with conduits model. The magmatic overpressure is set of 10 MPa for the deep
.005 chamber, 5 MPa for the shallower one.

.006

.007

.008

.009

.010

.011

.012

.013

.014

.015

.016

.017

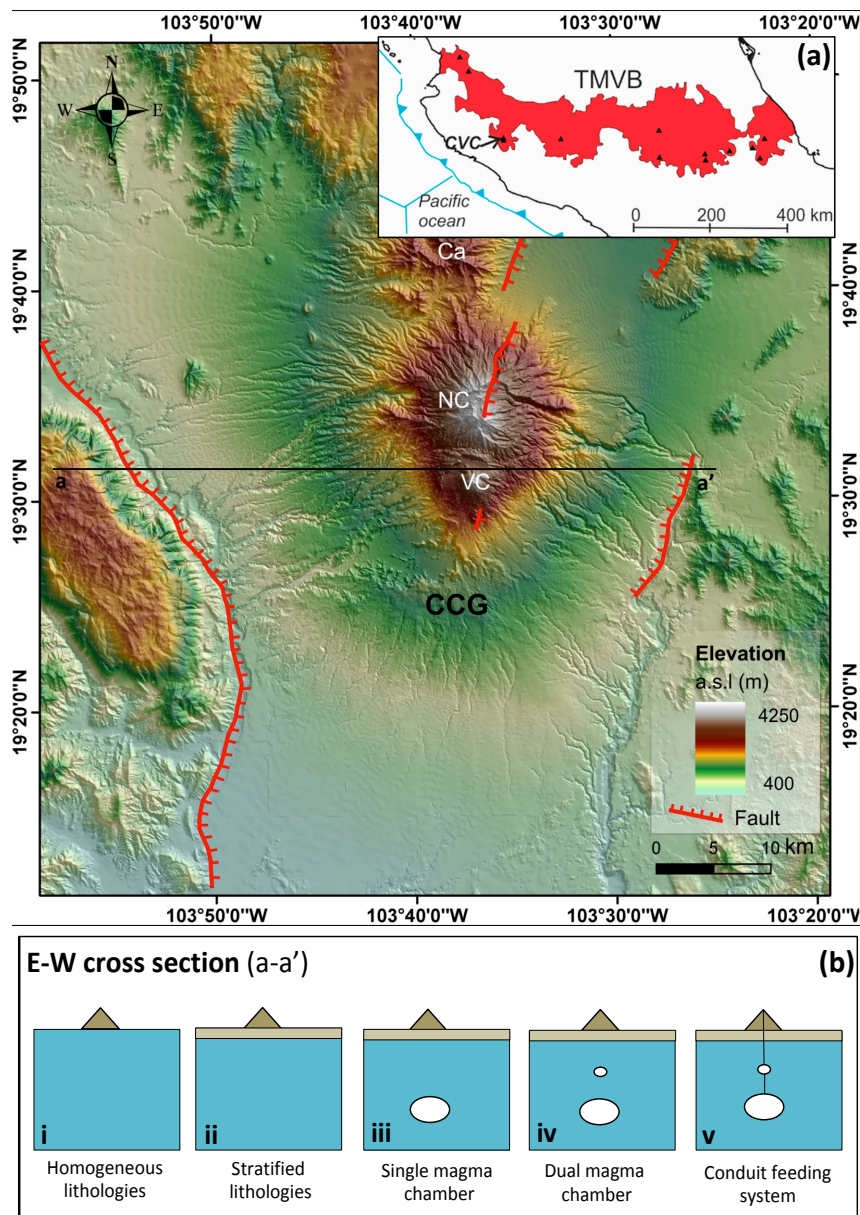
.018

.019



.020

.021 **Fig. 1**



.022

.023

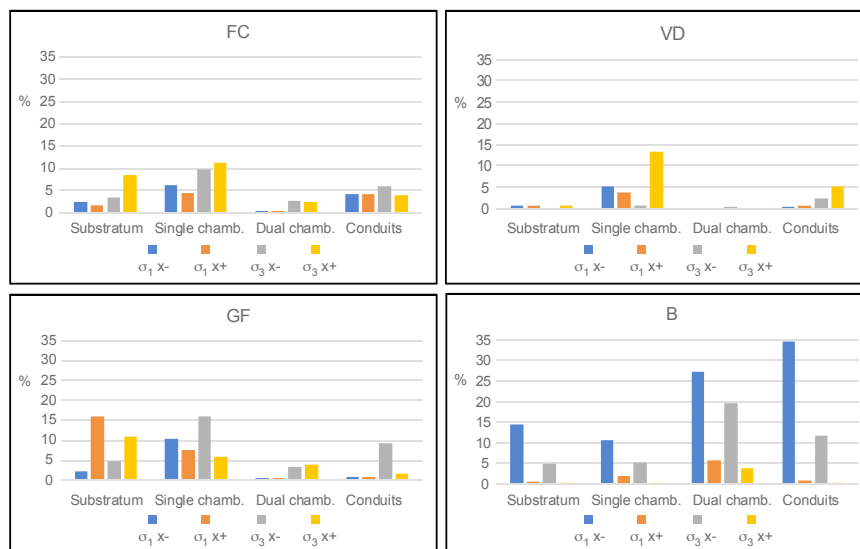
.024

.025



.026

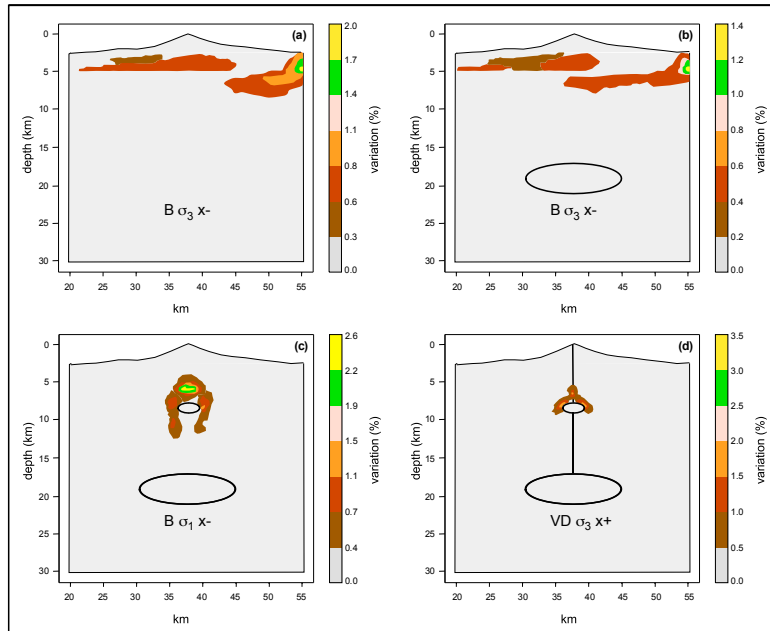
.027 **Fig. 2**



.028

.029

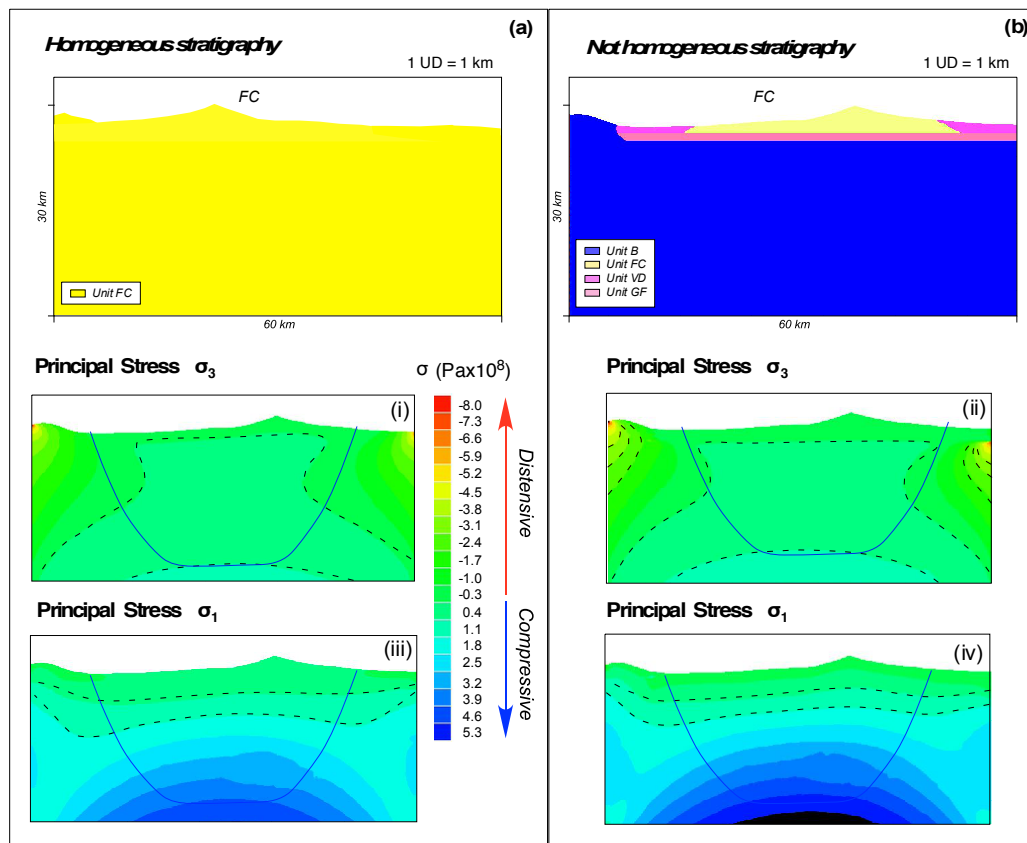
.030 **Fig. 3**



.031

.032

.033 **Fig. 4**



.034

.035

.036

.037

.038

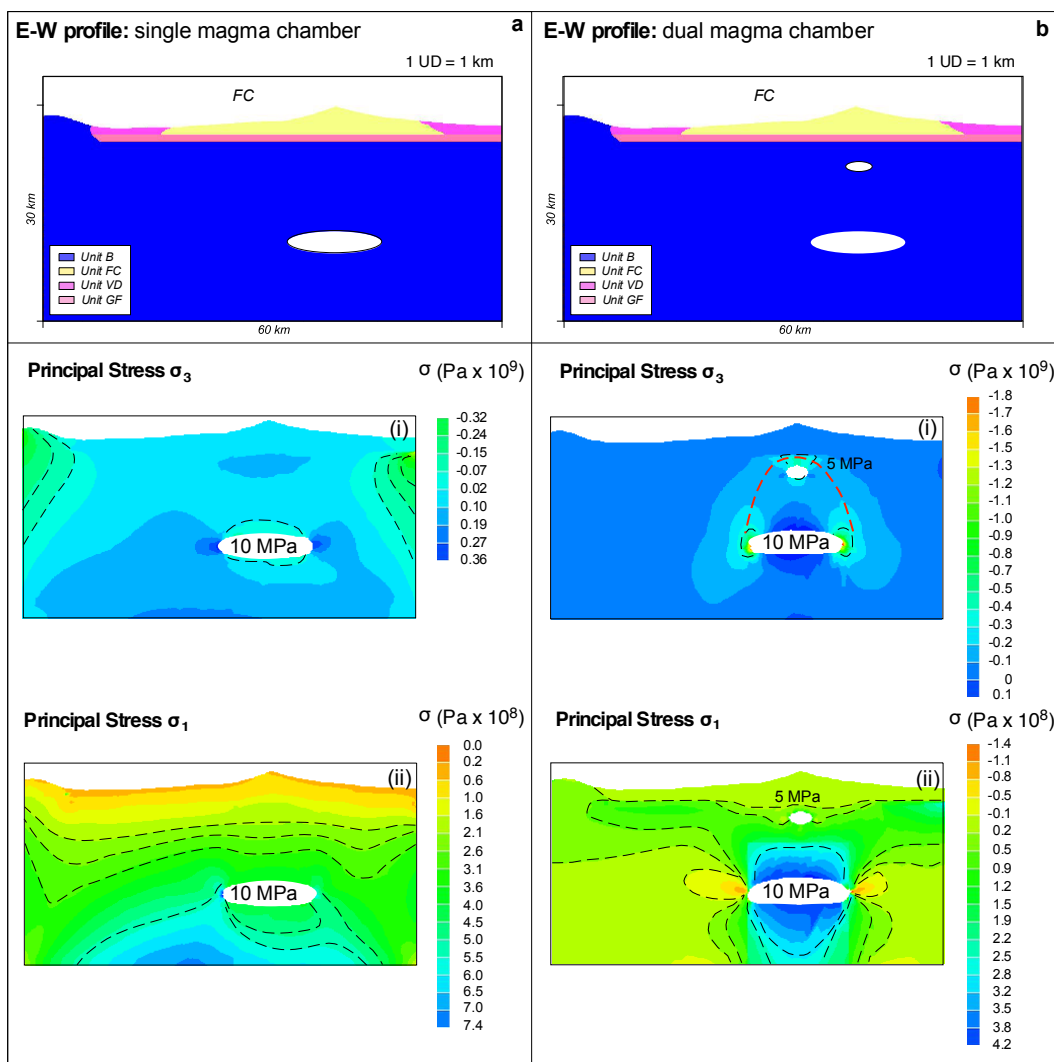
.039

.040

.041

.042

.043 Fig. 5



.044

.045

.046

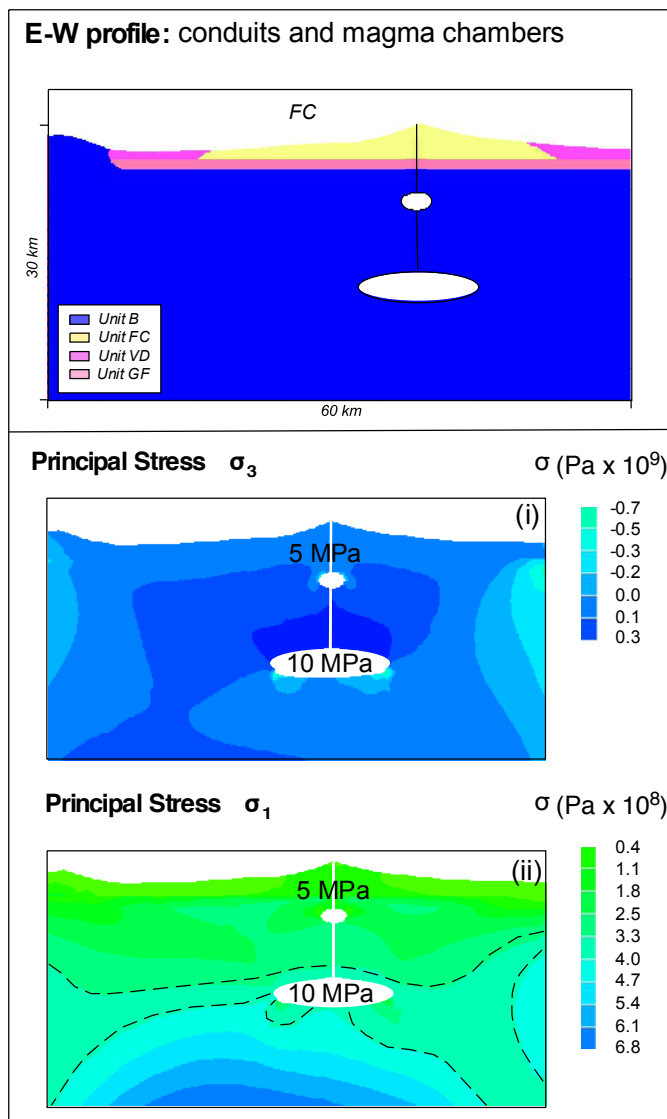
.047

.048

.049

.050

.051 **Fig. 6**



.052

.053

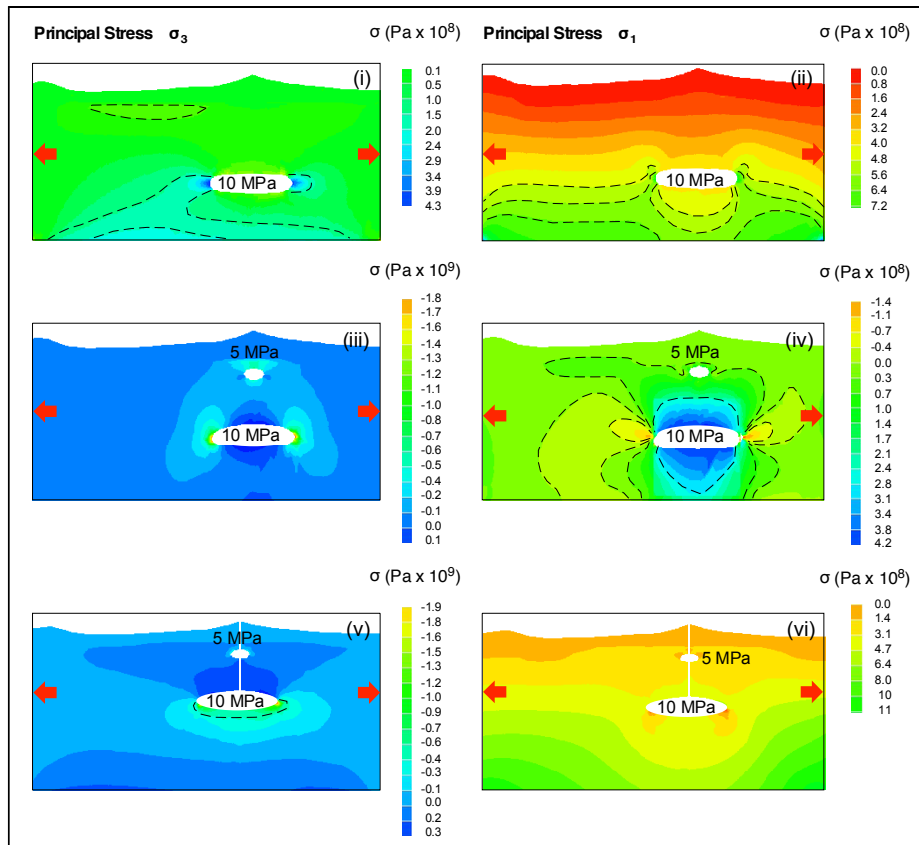
.054

.055

.056

.057

.058 **Fig. 7**



.059

.060

.061

.062

.063

.064

.065

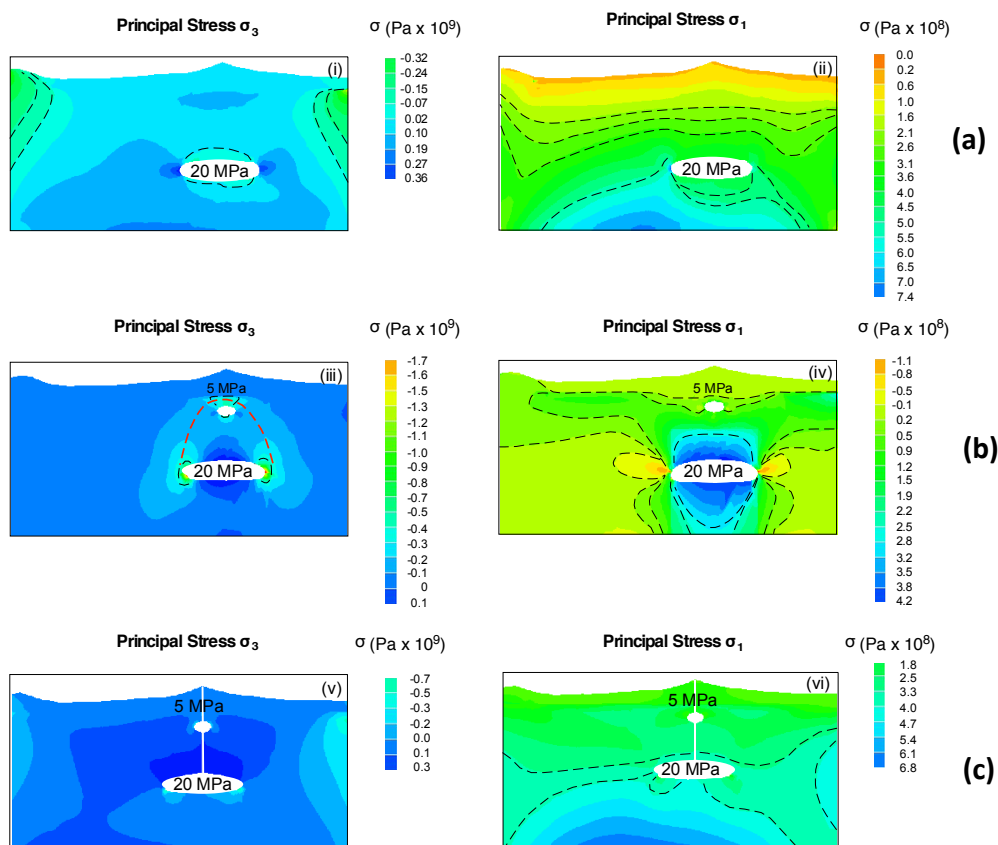
.066

.067

.068 **Appendix 1**



.069



.070

.071

.072

.073

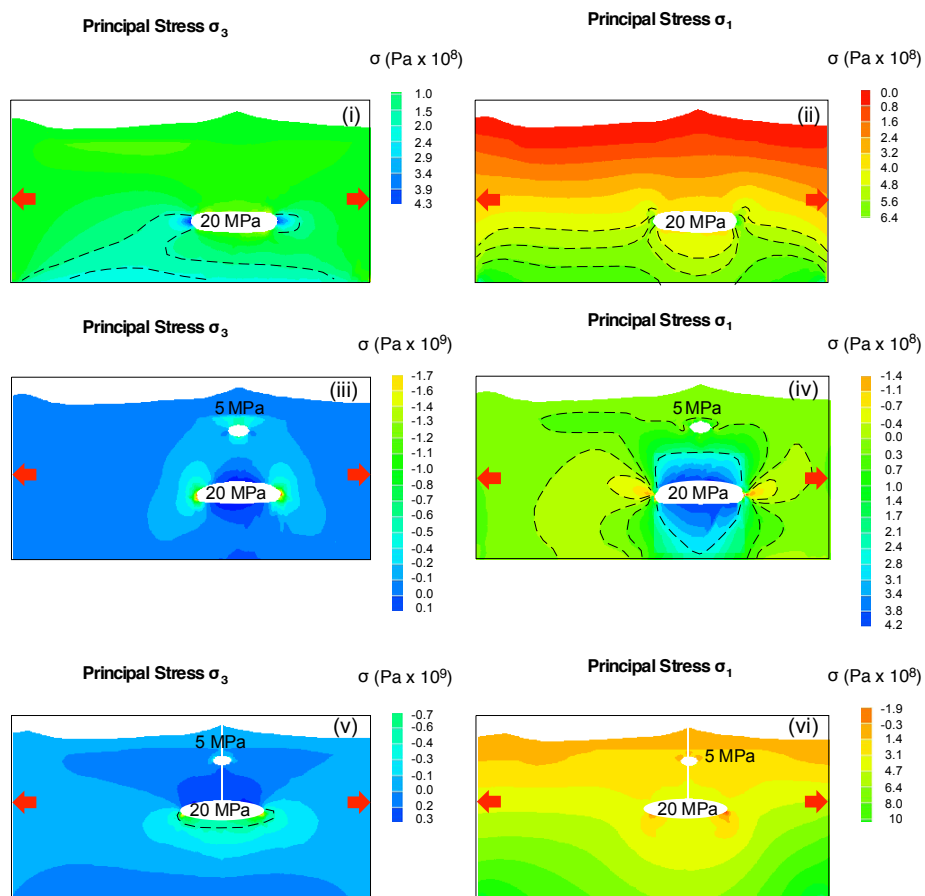
.074

.075

.076

.077

.078 Appendix 2



.079